forests

MDPI

Article

Quantifying Multi-Scale Carbon Sink Capability in Urban Green Spaces Using Integrated LiDAR

Yuhao Fang, Wenling Song, Yilun Cao, Shuge Su and Yuning Cheng *

School of Architecture, Southeast University, Nanjing 210096, China; fangyuhao@seu.edu.cn (Y.F.); wenlingsoong@163.com (W.S.); yilun@seu.edu.cn (Y.C.); 230248002@seu.edu.cn (S.S.)
* Correspondence: cyn999@126.com

Abstract

Urban green spaces play a vital role in climate change mitigation through carbon sequestration and storage. However, accurately quantifying their carbon sink capability remains challenging due to complex vertical structures and spatial heterogeneity. This study proposes a comprehensive inventory framework integrating multi-source LiDAR (UAV and Backpack) with a phenology-based complementary strategy to quantify carbon dynamics across three nested scales: green space types, plant communities, and species. Two key indicators—Carbon Sequestration Efficiency (CSE) and Carbon Density (CD)—were used to evaluate both the dynamic and static aspects of carbon sink function. The results reveal a clear asynchrony between CSE and CD across scales. No single plant type performed best in both dimensions, indicating a trade-off between growth efficiency and biomass accumulation. Hierarchical clustering identified distinct plant groups with divergent carbon sink strategies, supporting nuanced vegetation selection. The dual-indicator and dual-platform approach proposed in this study advances our existing understanding of the carbon sequestration capacity of urban green spaces and provides a robust methodological foundation for data-driven low-carbon urban ecological planning.

Keywords: urban green spaces; carbon sequestration; carbon storage; multi-scale and multi-dimensional differences; backpack and UAV LiDAR

1. Introduction

With the advancement of the "carbon peaking and carbon neutrality" strategy, green spaces have become vital components of urban carbon sinks. Their carbon sequestration and storage functions play a key role in mitigating urban carbon emissions [1,2]. However, their carbon sink capability varies significantly across spatial scales and structural dimensions. This heterogeneity arises from differences in green space types, community structures, and vertical vegetation complexity [3]. This heterogeneity across scales and dimensions complicates accurate assessment of the carbon sink capability of urban green spaces [4].

Current methodologies for assessing carbon sinks in urban green spaces face significant challenges in balancing spatial coverage with structural precision [5,6]. Field inventory methods, while accurate for individual trees, are labor-intensive and difficult to scale up for city-wide mapping [7]. Conversely, remote sensing approaches (e.g., optical imagery, satellite LiDAR) offer broad coverage but suffer from coarse resolution and mixed-pixel issues in fragmented urban patches, failing to capture the complex vertical stratification

Check for updates

Academic Editor: Lei Wang

Received: 25 November 2025
Revised: 23 December 2025
Accepted: 25 December 2025
Published: 26 December 2025

Copyright: © 2025 by the authors. Licensee MDPI, Basel, Switzerland. This article is an open access article distributed under the terms and conditions of the Creative Commons Attribution (CC BY) license.

characteristics of managed landscapes [8]. Similarly, flux-based methods (e.g., eddy covariance), despite being the gold standard for ecosystem-scale CO_2 exchange, provide only aggregate fluxes over large footprints, making it impossible to disentangle the specific contributions of heterogeneous plant communities [9]. Furthermore, process-based models (e.g., i-Tree) and assimilation methods often rely on generalized allometric equations or leaf-level photosynthetic rates, which may lack the precise, site-specific 3D canopy inputs (such as leaf area density and crown volume) needed to accurately reflect the structural variability of pruned and managed urban vegetation [10]. Consequently, there is an urgent need for a hybrid approach that integrates the structural fidelity of inventory methods with the efficiency of remote sensing to achieve high-resolution carbon accounting in complex urban environments.

To address these challenges, integrating stratified sampling with multi-source LiDAR technology provides a robust solution for the rapid and precise inventory of urban vegetation carbon sink capability. Previous studies have laid the technical groundwork for this hybrid approach: satellite LiDAR has demonstrated the potential for biomass mapping at coarse scales [11], while UAV LiDAR offers flexible canopy characterization suitable for rapid area mapping [12]. Complementarily, ground-based and backpack LiDAR systems have proven effective for high-resolution understory and trunk modeling [13,14]. However, relying on any single platform fails to capture the complete vertical profile required for accurate urban carbon sink accounting. By coupling a representative sampling strategy with the fusion of top down (UAV) and bottom–up (Backpack) data, this study proposes a comprehensive framework that overcomes the efficiency bottlenecks of traditional fieldwork while resolving the occlusion issues of remote sensing. This methodological integration enables the construction of high-fidelity 3D models, facilitating the simultaneous assessment of carbon storage and sequestration across the complex horizontal and vertical structures of urban green spaces.

This study aims to (1) Establish a high-precision, multi-source inventory framework that integrates stratified sampling, dual-platform LiDAR fusion, and phenology-based extraction to reconstruct the complete 3D structure of urban vegetation; (2) Quantify the multi-scale heterogeneity of Carbon Storage (CS), Carbon Density (CD), Carbon Sequestration (CSeq) and Carbon Sequestration Efficiency (CSE) across individual tree, community, and green space levels, revealing the scale-dependent patterns of carbon allocation; and (3) Identify high-performance functional types (species and communities) to provide actionable, data-driven guidelines for low-carbon urban green space design.

The novelty of this study lies in the synergistic integration of multi-source LiDAR (UAV + Backpack) and a phenology-based complementary strategy (Winter Stem + Summer Canopy). Unlike traditional single-snapshot assessments, this dual-indicator system captures the asynchronous variations between carbon stock and flux across complex spatial and vertical dimensions. This approach addresses the critical gap in capturing functional–structural mismatches, providing a refined technical basis for precise urban carbon accounting.

2. Data and Methods

This study focuses on urban green spaces in Nanjing, integrating backpack LiDAR, UAV LiDAR, and canopy analyzer data to construct high-resolution 3D vegetation models. Ecological parameters were obtained through field surveys and literature, and carbon sink indicators were calculated using established formulas. Carbon sink capability was analyzed across three spatial scales (green space, community and individual tree) and two structural dimensions (horizontal and vertical). Variation patterns and their drivers were identified

to inform carbon-efficient urban green space planning. The research framework is shown in Figure 1.

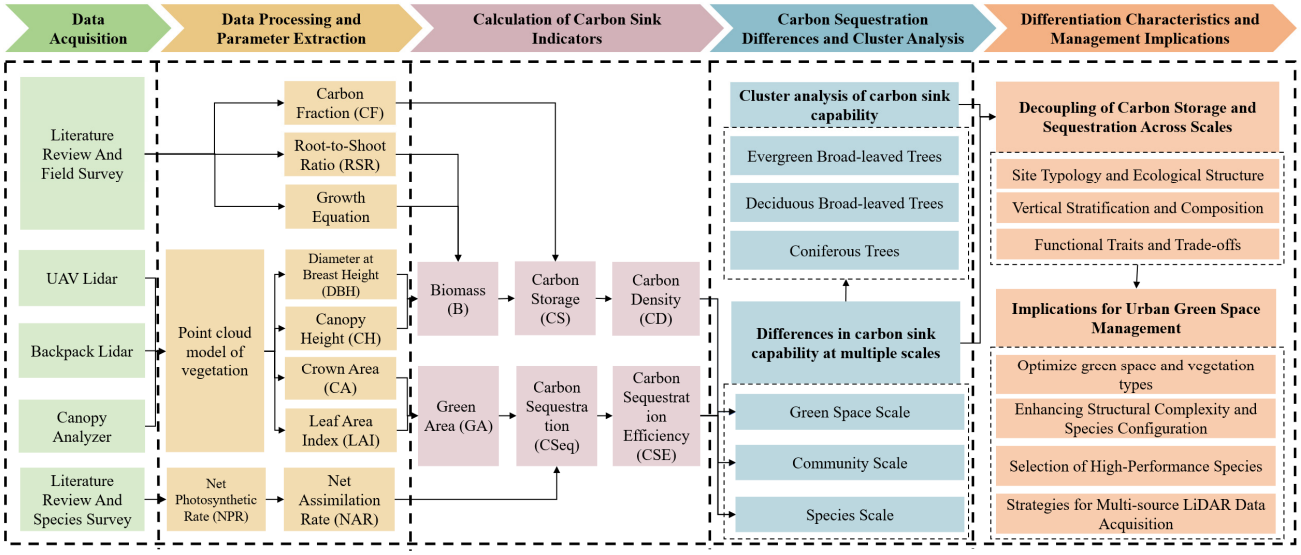

Figure 1. Research framework.

2.1. Study Area and Sampling

This study was conducted in the central urban area of Nanjing, a region characterized by a northern subtropical monsoon climate. The urban vegetation comprises a heterogeneous mix of evergreen and deciduous broadleaf forests. Given the high spatial heterogeneity of urban green spaces [15], a stratified purposive sampling strategy was adopted to ensure data representativeness and cost-effectiveness [16].

Site Selection (Stratum 1): We selected 20 urban green spaces stratified by park type (comprehensive parks, community parks, and specialized gardens), and vegetation coverage. This selection aimed to capture the full gradient of community structures and carbon sink capacities across the city.

Community Sampling (Stratum 2): Within the selected green spaces, a total of 445 plant communities were surveyed using a random sampling design. Standardized plots of 20 m × 20 m were established for each community. This plot dimension (400 m^2) was selected based on the concept of 'minimal area' in vegetation ecology, which suggests that a sampling area of 200–500 m^2 is required to adequately capture the species composition and structural complexity of the arboreal layer in temperate to subtropical forests [17]. The sampling effort was weighted by the total green area of each site to ensure a minimum sampling intensity of 10%. This proportion significantly exceeds the typical sampling density employed in city-scale urban forest assessments (e.g., often <1% in standard i-Tree protocols) [18]. By adopting this high-intensity sampling strategy, we aimed to rigorously capture the fine-scale structural heterogeneity and species diversity characteristics of fragmented urban vegetation patches, thereby balancing statistical robustness with operational feasibility.

Detailed characteristics of the selected sites and the distribution of sampled communities are provided in Figure 2 and Table A1.

2.2. Data Acquisition

2.2.1. Dual-Platform LiDAR Survey

LiDAR data collection was conducted across a dual-platform strategy which employed to ensure complete vertical coverage of the vegetation structure:

(1) Backpack LiDAR (Understory): An OSlam RTK-SLAM-R6 system was used to scan the understory and tree trunks. This system integrates RTK and SLAM technologies to provide high-density point clouds (relative accuracy: 2–4 cm) in GNSS-denied environments, such as beneath dense canopies where UAV signals are obstructed.

(2) UAV LiDAR (Canopy): A DJI MATRICE 350 RTK UAV (Da-Jiang Innovations, Shenzhen, China) equipped with a Zenith L2 sensor was deployed to map the upper canopy surface. The UAV platform utilized RTK positioning to ensure centimeter-level absolute geolocation accuracy, complementing the ground-based backpack data.

Data collection was conducted across two phenologically distinct phases: Winter (Jan–Feb 2024, leaf-off) and Summer (Jun–Jul 2024, leaf-on). Daily acquisition windows were restricted to 08:00–12:00 and 14:00–18:00 to minimize atmospheric interference.

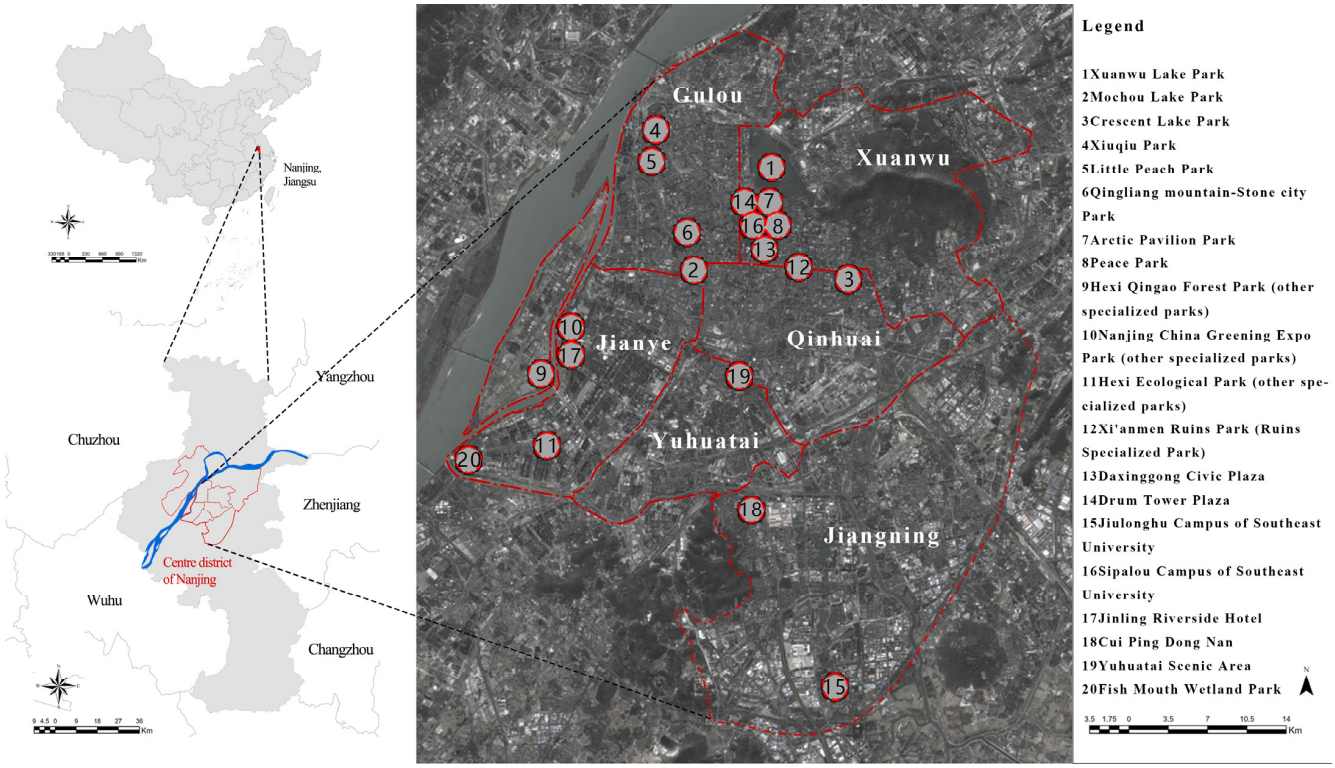

Figure 2. Study area and samples.

2.2.2. Field Measurements

Concurrent with the summer LiDAR campaign, detailed field surveys were conducted to validate species composition and acquire physiological parameters. In each sample plot, the southwest corner was geolocated using RTK-GPS to ensure precise alignment with the LiDAR data. Vegetation inventory recorded species composition, abundance, and vertical structure across tree, shrub, and ground cover layers.

Based on the dominance of evergreen versus deciduous and coniferous versus broadleaf species, the 445 communities were categorized into 15 functional types, the detailed classification system and abbreviations for which are provided in Abbreviations.

To quantify canopy functional traits, a DC-2000 Canopy Analyzer (Shijiazhuang Fansheng Technology Co., Ltd., Shijiazhuang City, China) was used to capture hemispherical canopy images at the center and four corners of each plot under diffuse light conditions. The Leaf Area Index (LAI) was subsequently derived using the device's proprietary image processing software, serving as a critical input for carbon sequestration modeling.

2.2.3. Acquisition of Ecological Parameters

To bridge the gap between structural morphology and carbon metrics, key ecological coefficients were derived from established standards and regional literature. The Root-to-Shoot Ratio (RSR) and Carbon Fraction were obtained from national industry standards (e.g., GB/T 43648-2024, LY/T 2988-2018) and guidelines specific to urban green space carbon measurement. For ornamental species lacking empirical data, default values were applied based on plant functional types (broadleaf or conifer), as detailed in Table A2. Additionally, the Net Photosynthetic Rate (NPR), reflecting the maximum photosynthetic efficiency, was sourced from peer-reviewed literature focusing on local climatic conditions and vegetation types in Nanjing. When species-specific data were unavailable, values from ecologically similar species were used as proxies. All compiled photosynthetic parameters were rigorously screened for ecological relevance and are listed in Table A3.

2.3. Data Processing and Feature Extraction

2.3.1. Multi-Platform Fusion and Registration

A robust workflow was implemented to integrate the multi-platform LiDAR data using Trimble RealWorks 12.

First, to eliminate vertical blind spots, the Backpack LiDAR point cloud (understory) was co-registered to the UAV LiDAR point cloud (canopy) using a coarse-to-fine strategy in Trimble RealWorks (Figure 3). The fusion quality was validated on 10 randomly selected sample plots. The resulting Root Mean Square Error (RMSE) ranged from 28 mm to 42 mm (mean: 35.3 mm), with a mean spatial overlap of 72%, ensuring precise geometric alignment for individual tree reconstruction.

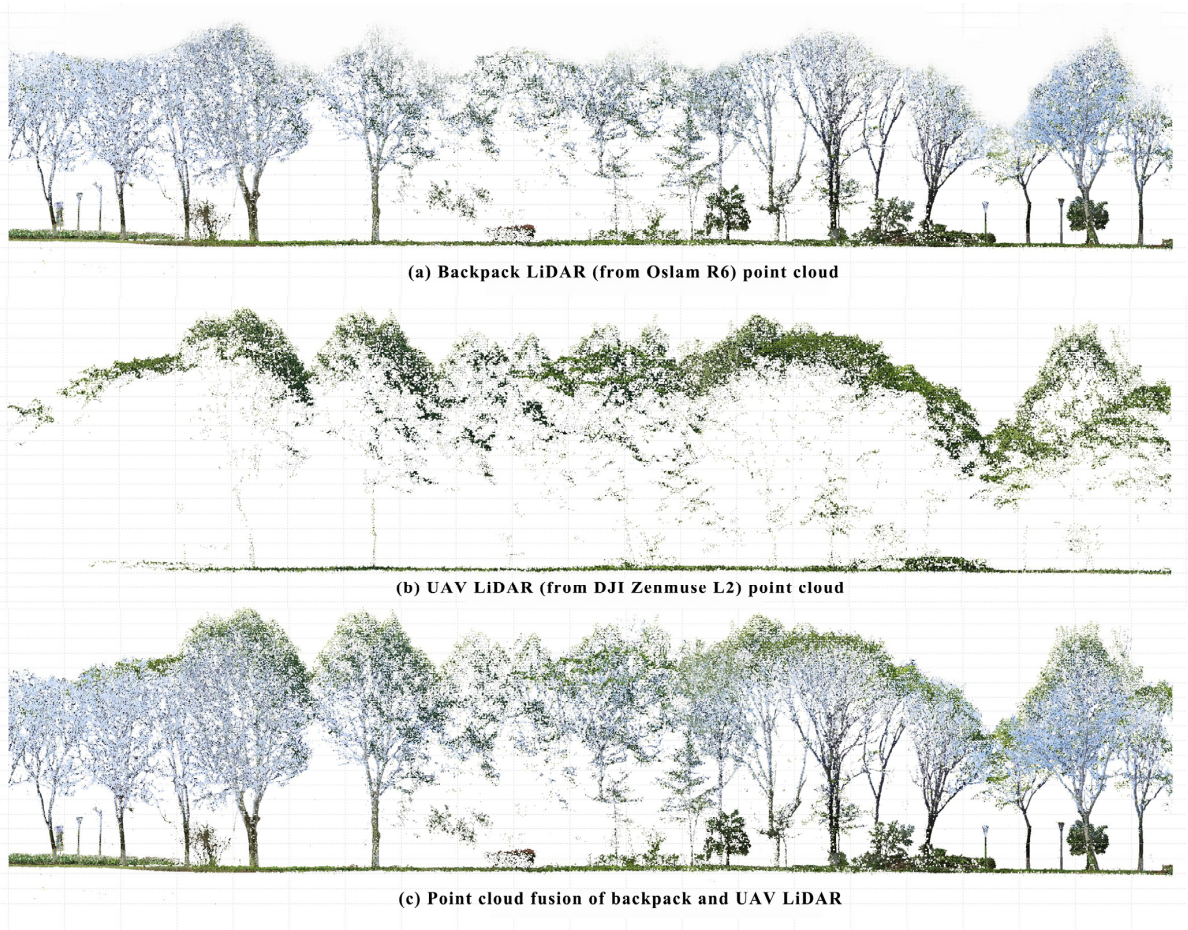

Figure 3. Fusion of backpack lidar and airborne lidar.

Second, regarding the multi-temporal datasets, we adopted a phenology-based complementary strategy rather than merging seasonal point clouds. Winter data (leaf-off) were used as the geometric baseline for extracting woody structures (e.g., stem location) to minimize occlusion, while Summer data (leaf-on) were used to characterize canopy functional traits (e.g., crown area). Following fusion and noise filtering, the integrated point clouds were normalized using a Digital Terrain Model (DTM) generated from the summer dataset.

2.3.2. Individual Tree Segmentation

After data fusion, individual trees were segmented from the point clouds using the seed-point-based algorithm within the LiDAR360 v5.2.2 software platform. The segmentation parameters were rigorously calibrated based on the high point density of the backpack sensor (~10,000 pts/m^2) and preliminary tests on representative plots. Specifically, the clustering threshold was set to 0.2 m. Given the average point spacing of approximately 1 cm, this threshold ensured robust connectivity within single canopies while effectively separating adjacent crowns. To filter out noise, the minimum cluster size was set to 500 points, which corresponds to a minimum effective surface area of roughly 0.05 m^2, thereby eliminating small artifacts such as suspended wires. Vertically, the ground height threshold was set to 0.3 m to accommodate the device's absolute positioning accuracy (3 cm) and effectively exclude low-lying vegetation and curbs. To strictly differentiate arboreal trees from the shrub layer, a minimum tree height of 2 m was applied. This threshold was selected based on our field investigations, which indicated that arboreal specimens in the study area typically exceed this height, and was further supported by relevant urban vegetation studies [19]. Finally, the DBH extraction range was constrained to 1.2–1.4 m, adhering to standard forestry practices for precise stem measurement. Figure 4 shows the results extracted by individual tree segmentation.

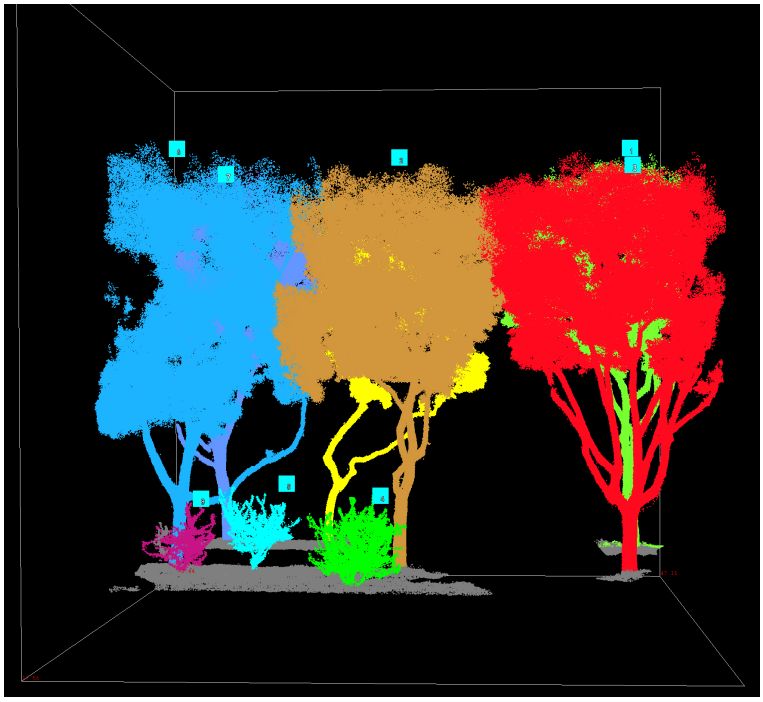

Figure 4. The effect of segmenting a point cloud community into individual trees. Colors indicate the separation results for different individual trees, while numbers denote tree IDs.

The segmentation accuracy was rigorously validated against field inventory records. For each community, Recall (r), Precision (p), and F-score (F) were calculated based on the

number of correctly segmented trees (TP), missed trees (FN), and falsely segmented trees (FP) (Equations (1)–(3)).

$$r = \frac{TP}{TP + FN} \quad (1)$$

$$p = \frac{TP}{TP + FP} \quad (2)$$

$$F = 2 \times \frac{r \times p}{r + p} \quad (3)$$

where r (recall) denotes the detection rate of trees, p (precision) denotes the correct rate of tree segmentation, and F (F-score) is the overall precision that integrates the wrong and missed scores, with all three varying between 0 and 1. TP is partitioned trees, FN is the number of missed trees, FP is the number of incorrectly partitioned trees.

Communities with an initial F-score < 0.8 underwent manual seed point adjustment and re-segmentation. Communities that failed to reach this threshold after adjustment were excluded. Ultimately, 393 out of 445 communities met the validity criteria (F-score $\geq$ 0.8), yielding an overall data qualification rate of 88.31%.

2.3.3. Phenology-Based Variable Extraction

Following individual tree segmentation, structural variables were automatically extracted. To maximize the accuracy of carbon metrics, we implemented a phenology-based selective extraction strategy (summarized in Table 1). Structural parameters sensitive to foliage occlusion, specifically Tree Location and DBH, were extracted from the Winter (leaf-off) dataset, where the absence of leaves provided clear visibility of tree trunks. Conversely, canopy-related parameters, including Canopy Height (CH), Crown Width (CW) and Crown Area (CA), were derived from the summer dataset, with the full canopy extent to capture maximum photosynthetic potential. Finally, the LiDAR-derived structural metrics were linked with the field-measured LAI and literature-derived ecological coefficients to form a complete dataset for carbon modeling.

Table 1. Data Category and Source.

Category	Variable	Data Source	Reference
Tree Structure	Canopy Height (CH)	LiDAR Point Cloud	Max value from fused UAV + Backpack data (Winter priority for stem top detection)
	Diameter at Breast Height (DBH)		Extracted from Winter point cloud to minimize occlusion
	Crown Width (CW)		Extracted from Summer point cloud for maximum canopy extent
	Crown Area (CA)		Calculated assuming a circular crown projection based on the average Crown Width (CW)
Physiology	Leaf Area Index (LAI)	Field Instrument	Measured using DC-2000 Canopy Analyzer during Summer
Carbon Estimation	Biomass (B)	Calculation	Estimated using allometric equations based on CH and DBH
	Root-to-Shoot Ratio (RSR)	Literature	Regional standard coefficients for specific tree species
	Carbon Fraction (CF)		Conversion factors (typically 0.45–0.50) based on species
	Net Photosynthetic Rate (NPR)		Species-specific photosynthetic rates from physiological studies

It is important to note that the CSE derived in this study represents the sequestration capacity during the peak growth season. All physiological measurements, specifically LAI, were conducted during the summer to capture the maximum photosynthetic potential of both evergreen and deciduous species. This temporal standardization ensures the comparability of metrics across different functional groups but does not account for the physiological dormancy of deciduous species during the winter season.

2.4. Carbon Sink Estimation Framework

Carbon sink capability was assessed through two complementary dimensions: Carbon Storage, representing the accumulated carbon pool, and Carbon Sequestration, representing the annual rate of CO_2 fixation.

2.4.1. Calculation of Carbon Storage

CS and CD were estimated for both individual plants and communities, incorporating above- and belowground biomass.

(1) Biomass (B) estimation

Biomass was calculated using species-specific allometric equations based on LiDAR-derived structural metrics. To ensure regional applicability, we selected equations developed specifically for urban tree species in East China (summarized in Table A3). The general forms of the models are as follows:

$$B_{ij} = a(DBH)^b \quad (4)$$

$$\text{Or } B_{ij} = a(DBH^2CH)^b \quad (5)$$

where B_{ij}—Biomass of organ j of tree species i in kilograms (kg); DBH—Diameter at breast height (cm); CH—Canopy height (m); a, b—Fitting coefficients.

Above- and belowground biomass of tree species i is calculated in Equation (6):

$$B_i = B_{gi} + B_{ugi} \quad (6)$$

where B_{gi}: Aboveground biomass of tree species i (kg); B_{ugi}: Underground biomass of tree species i (kg); B_i: Whole-plant biomass of tree species i (kg); Aboveground biomass includes the biomass of the trunk, branches, and leaves; underground biomass includes root biomass.

(2) Carbon storage (CS) calculation

CS can be derived from the product of biomass and carbon fraction, calculated by Equation (7).

$$CS = B \times CF \quad (7)$$

where CS is the carbon storage (kgC); B is the biomass (kgC); CF is the carbon fraction, dimensionless.

(3) Carbon density (CD) calculation

CD is the amount of carbon contained per unit volume or unit area, and is obtained by dividing the carbon stock by the volume of a single tree or the area of a community. The former is used to measure the carbon sequestration capability of a single tree of landscape garden plants, and the latter is used to measure the carbon sequestration capability of a community over a long period of time, and is calculated by Equation (8).

$$CD = CS \div S \quad (8)$$

where CD is carbon density (kgC · m^{-2}); CS is carbon storage (kgC); S is community area (m^2).

2.4.2. Calculation of Carbon Sequestration

Carbon sequestration metrics quantify the ability of plants to fix CO_2. These metrics are derived using green area and net assimilation rate.

(1) Green area (GA)

GA represents the photosynthetically active surface. For trees, green area is calculated as the product of canopy area and leaf area index, while for shrubs and herbaceous layers, the leaf area index is multiplied by ground coverage area. The formula is shown in Equation (9):

$$GA = \mathrm{LAI} \times \mathrm{CA} \quad (9)$$

where GA is the green area (m^2); LAI is the leaf area index, dimensionless; CA is the canopy area/covered area (m^2).

(2) Net assimilation rate (NAR)

The NAR estimates the daily net CO_2 uptake per unit leaf area. We derived NAR from species-specific Net Photosynthetic Rates (NPRs) sourced from the literature (Table A4). To account for the disparity between leaf-level potential and canopy-level reality, two correction factors were applied:

Canopy Light Attenuation (θ): A coefficient of 0.5 was applied to convert the maximum leaf-level photosynthetic rate to the mean canopy-level rate. This threshold is derived from established literature [20,21], which indicates that due to canopy self-shading and the vertical extinction of light (following the Beer–Lambert law), the average photosynthetic efficiency of the entire canopy is approximately 50% of the light-saturated rate measured at the sun-exposed upper leaves.

Dark Respiration (ω): A coefficient of 0.8 was applied to deduct nighttime respiratory carbon loss (assumed to be 20% of daytime assimilation) [22].

The daily NAR is calculated as follows:

$$NAR = NPR \times 10 \times 3600 \div 10^6 \times 44 \times \theta \times \omega \quad (10)$$

where NAR is the net assimilation rate (gCO_2 · m^{-2} · d^{-1}); NPR is the net photosynthetic rate obtained from literature (μmolCO_2 · m^{-2} · s^{-1}); 10 represents the effective daytime duration for photosynthesis (from 8:00 to 18:00, in hours); 3600 is the number of seconds per hour; 10^6 is the conversion factor from μmol to mol; 44 is the molar mass of CO_2; θ is the canopy-scale light attenuation coefficient, set to 0.5; and ω is the correction factor accounting for respiratory carbon loss during nighttime, set to 0.8.

(3) Carbon sequestration (CSeq)

CSeq is defined as the net uptake of atmospheric CO_2 by landscape vegetation through photosynthesis, after subtracting respiratory losses, and is expressed in kilograms of CO_2 (kg CO_2).

Following the principle of net assimilation, daily CSeq was calculated as the product of green area and net assimilation rate, as defined in Equation (11):

$$CSeq_{daily} = NAR \times GA \div 10^3 \quad (11)$$

where $CSeq_{daily}$ is the amount of carbon sequestered (kgCO_2 · d^{-1}); NAR is net assimilation rate (gCO_2 · m^{-2}); GA is the amount of green (m^2); and 10^3 is the unit conversion factor from g to kg.

Since net assimilation rate is calculated on a daily basis, annual CSeq needs to be multiplied by the number of days of effective photosynthesis. Nanjing is located at the northern edge of the subtropical monsoon climate zone, characterized by abundant rainfall and high summer temperatures. During the hottest periods, photosynthetic activity may be partially suppressed, the number of effective photosynthetically active days per year is estimated to range from 220 to 260. In this study, we conservatively set the annual effective photosynthetic duration to 240 days. Annual CSeq can then be estimated by multiplying the daily CSeq by the number of effective photosynthetic days, as defined in Equation (12):

$$CSeq_{annual} = CSeq_{daily} \times 240 \quad (12)$$

where $CSeq_{annual}$ is the annual carbon sequestration ($kgCO_2 \cdot yr^{-1}$); $CSEQ_{daily}$ is the daily carbon sequestration ($kgCO_2$); 240 is the days of annual effective photosynthetic duration.

(4) Carbon sequestration efficiency (CSE)

CSE is the annual carbon sequestration per unit area and is used to measure the efficiency of carbon sequestration by different vegetation, as defined in Equation (13):

$$\text{CSE} = CSeq_{annual} \div A \quad (13)$$

where CSE is the carbon sequestration efficiency ($kg\ CO_2 \cdot m^{-2} \cdot yr^{-1}$), $CSeq_{annual}$ is the annual carbon sequestration ($kg\ CO_2 \cdot m^{-2} \cdot yr^{-1}$); A is the footprint or canopy area of the vegetation (m^2).

To facilitate comparison with carbon storage, this study uniformly converted all carbon sink indicators to kgC.

2.5. Accuracy Validation

To evaluate the accuracy of the multi-source LiDAR extraction, field validation was performed on 50 randomly selected trees. Ground truth data were collected using standard forestry methods: DBH was measured using a diameter tape; CH was measured using a laser hypsometer; and CW was determined by averaging two perpendicular measurements of the crown projection. The accuracy assessment (Figure 5) compares the LiDAR-derived metrics against these field measurements. The results are as follows:

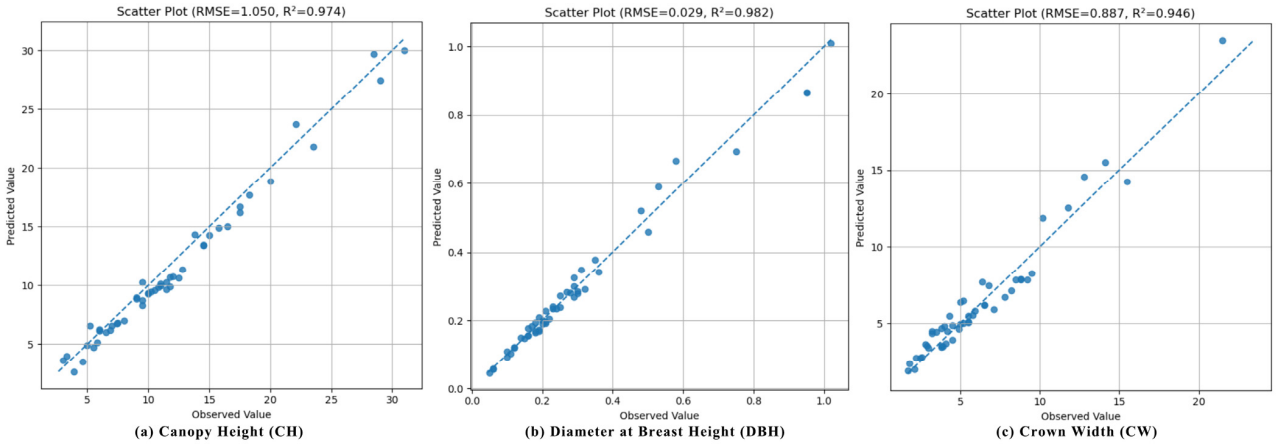

Figure 5. Point cloud measurement accuracy evaluation based on three indicators.

CH: The extraction achieved an RMSE of 1.05 m with an R^2 of 0.974, demonstrating effective canopy top detection.

DBH: The RMSE was 2.9 cm (0.029 m) with an R^2 of 0.982, indicating high precision in stem reconstruction.

CW: The RMSE was 0.89 m with an R^2 of 0.946.

These results confirm that the fused LiDAR data provide precise geometric inputs for carbon estimation. The observed error margins are consistent with recent international benchmarks for mobile laser scanning inventories [23,24], which typically report DBH RMSE values of 1–4 cm and height errors of 0.5–1.5 m as reliable for plot-level biomass estimation.

2.6. Statistical Analysis

Statistical analyses were conducted using SPSS 27.0 to quantify carbon sink differences across scales and identify functional vegetation types.

(1) Data Screening and Descriptive Statistics

To ensure the robustness of the comparison, the dataset was filtered to retain the most representative urban vegetation. A total of 38 multi-species community types and 153 common tree species (comprising 25 evergreen broadleaf, 105 deciduous broadleaf, and 23 coniferous species) were selected for the final analysis.

We calculated the Standard Deviation (SD), and Coefficient of Variation (CV) for CD and CSE. The CV was specifically used to quantify the degree of heterogeneity in carbon sink capability within and between different green space types and community structures.

(2) Hierarchical Clustering for Typology

To categorize the diverse vegetation into manageable functional groups based on their carbon performance, Hierarchical Clustering was employed. We used CD and CSE as the dual input variables to capture both the CS and CSeq dimensions. The clustering utilized Ward's method with Squared Euclidean distance, which is effective in identifying compact, spherical clusters. This analysis aimed to classify species and communities into distinct levels (e.g., High, Medium, Low) of carbon sink capability, providing a simplified typology for urban green space planning.

3. Results

3.1. Multi-Scale Assessment of Carbon Sink Capability

3.1.1. Green Space Scale

Significant variations in carbon sink capability were observed across the four functional green space types, forming a clear hierarchical gradient as shown in Table 2. Regional green spaces functioned as the primary urban carbon reservoirs, recording the highest values for both CD (10.80 kg C $\cdot$ m^{-2}) and CSE (1.44 kg C $\cdot$ m^{-2} $\cdot$ yr^{-1}). Their storage capability was approximately 1.5 times that of park green spaces and over 3.5 times that of plaza green spaces, reflecting the benefits of large-scale, undisturbed vegetation structures. Following regional spaces, Affiliated green spaces and Park green spaces constituted an intermediate tier. In contrast, Plaza green spaces consistently demonstrated the lowest performance metrics, likely constrained by fragmented vegetation patches and extensive impervious surfaces.

Table 2. Carbon sink capability of four typical types of urban green spaces.

No.	Green Space Types	Number of Green Spaces	CSE (kgC $\cdot$ m^{-2} $\cdot$ yr^{-1})	CD (kg C $\cdot$ m^{-2})
1	Park	12	1.17	6.07
2	Plaza	2	0.95	3.08
3	Affiliated	4	1.20	7.12
4	Regional	2	1.44	10.80

Detailed analysis of the 20 individual sites further revealed substantial intra-group heterogeneity (Figure 6). Within the regional category, the Yuhuatai Scenic Area achieved the highest overall CD (9.70 kg C · m^{-2}) among all surveyed sites, primarily driven by its extensive cover of mature evergreen forests. For affiliated spaces, the carbon capability varied significantly with land use history. For instance, the Sipalou Campus of Southeast University, characterized by mature tree stands, recorded a carbon density of 10.05 kg C · m^{-2}, rivaling that of regional scenic areas. Conversely, newer residential sites like Cui Ping Dong Nan exhibited much lower storage values (3.53 kg C · m^{-2}), indicating the strong influence of stand age on carbon accumulation.

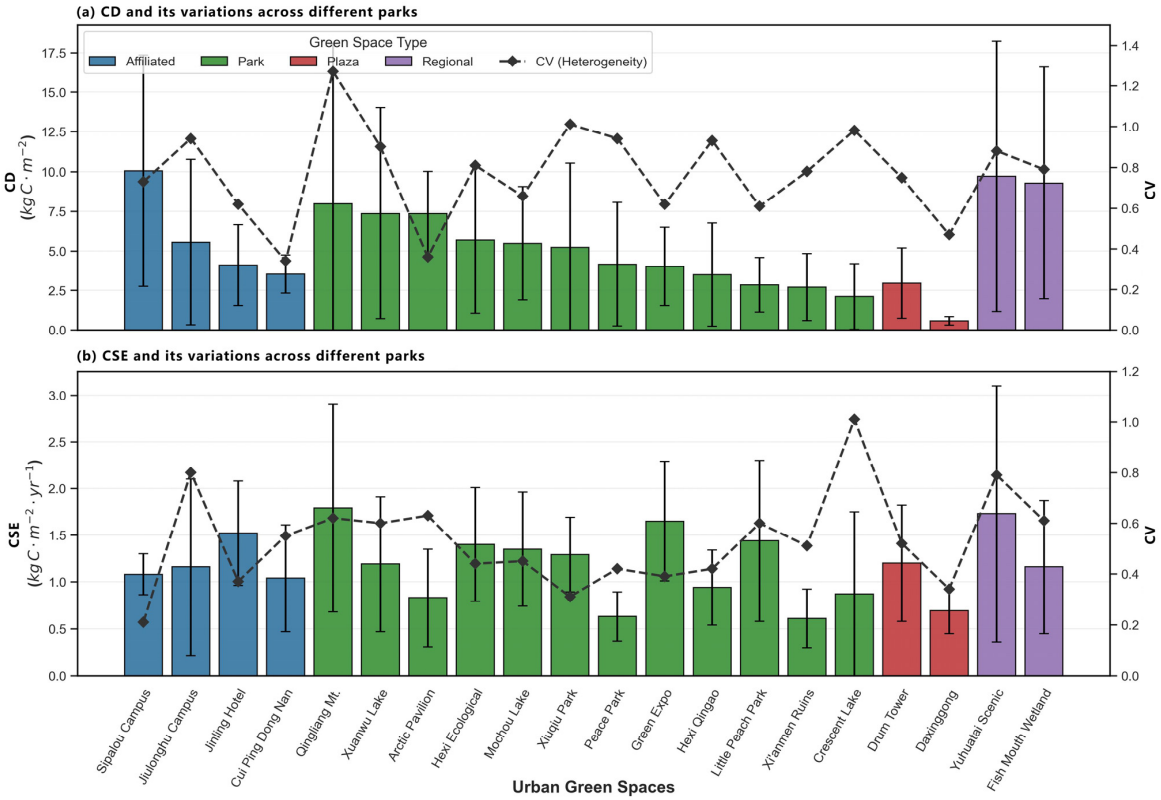

Figure 6. Variations in CD and CSE across different parks. (**a**) Variations in CD across parks and (**b**) variations in CSE across parks. The colored bar charts display the mean values for each park and are grouped by green space types (parks, squares, attached green spaces, and regional green spaces). Error bars indicate the SD. The dashed lines on the secondary y-axis represent the CV to reflect the spatial heterogeneity of the vegetation structure within each site.

Similar variability was evident within park green spaces, where performance appeared linked to park themes and topography. Mountain-type parks such as Qingliang Mountain and waterfront parks like Xuanwu Lake significantly outperformed smaller neighborhood parks such as Peace Park. Specifically, the CD in these complex ecological parks was nearly double that of the simplified recreational parks. These findings suggest that green spaces with complex terrain or proximity to water bodies may support more biomass-rich communities compared to flat, highly managed urban parks.

The SD and CV provide insights into the internal heterogeneity of these spaces. Naturalistic sites like mountain parks displayed higher variability (e.g., Qingliang Mountain CD_CV = 1.27), reflecting a diverse mosaic of dense forests and open spaces. Conversely, managed environments like campuses and residential areas exhibited lower CV values (e.g., Sipalou CES_CV = 0.21), indicating more uniform planting patterns and standardized maintenance regimes.

3.1.2. Communities Scale

Community configuration significantly influenced carbon sink capability. Specifically, the combination of species composition and vertical layering drove distinct differences in both efficiency and stability (Figure 7).

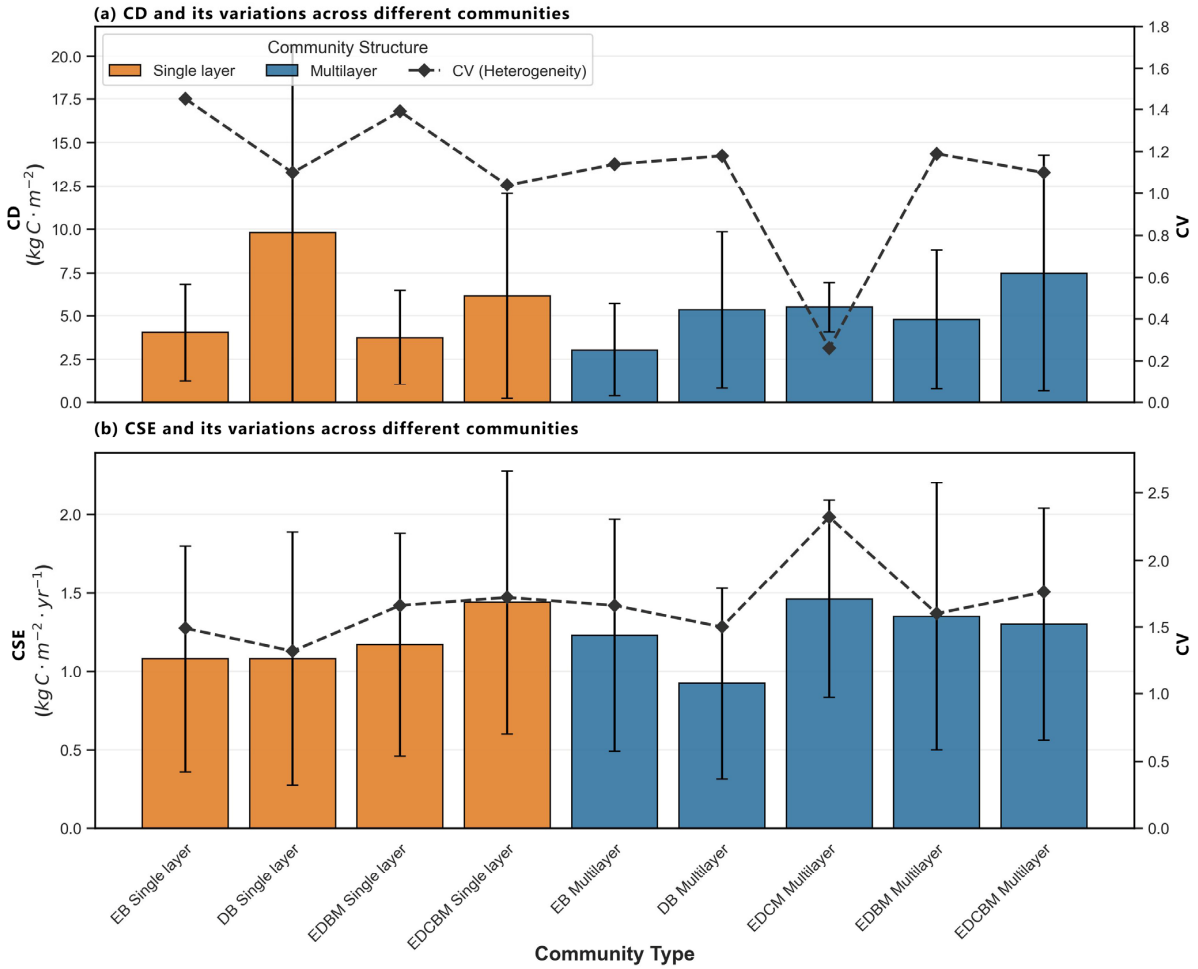

Figure 7. Variations in CD and CSE across different plant communities. (**a**) Variations in CD across community types and (**b**) variations in CSE across community types. The colored bar charts display the mean values grouped by community type. Error bars indicate the SD. The dashed lines on the secondary y-axis represent the CV to reflect the heterogeneity of carbon sequestration capacity among community types.

Functional mixing appeared to be the primary driver of carbon flux. Communities that integrated diverse functional traits, such as the mixed Evergreen-Deciduous Conifer-Broadleaf Mixed Forest (EDCBM) and Evergreen-Deciduous Conifer Mixed Forest (EDCM) types, consistently achieved higher sequestration rates exceeding 1.30 kg $C \cdot m^{-2} \cdot yr^{-1}$. These mixed groups outperformed simpler structures like pure Deciduous Broadleaf (DB) or Evergreen Broadleaf (EB) communities. This suggests that combining different plant types enhances annual carbon uptake capabilities regardless of whether the structure is single-layer or multilayer.

Vertical complexity acted as a factor in stabilizing carbon distribution. Single-layer communities generally showed higher spatial heterogeneity. For instance, single-layer Evergreen Broadleaf Forest (EB) and Evergreen–Deciduous Broadleaf Mixed Forest (EDBM) types exhibited CV_CD values ranging from 1.39 to 1.45, indicating that simplified vertical structures tend to form less predictable carbon pools. Conversely, multilayer communities demonstrated superior stability. The Multilayer EDCBM and DB communities maintained

moderate to high carbon stocks while keeping spatial variability lower, with CV_CD values clustered around 1.10 to 1.18. The EDCM Multilayer community showed exceptional homogeneity with a CV_CD of 0.26, but this specific result implies a need for cautious interpretation due to the small sample size (n = 5).

Overall, single-layer DB communities provided the highest absolute carbon density but lacked the high functional efficiency of mixed stands. The Multilayer EDCBM configuration emerged as a balanced option that delivers high sequestration efficiency combined with reliable and spatially stable carbon storage.

3.1.3. Species Scale

To understand the carbon sink capability of different trees, we analyzed 5016 individual trees across 145 species, categorized into three distinct life forms (Figure 8). The results revealed a clear divergence between carbon storage capability and sequestration rate among functional types.

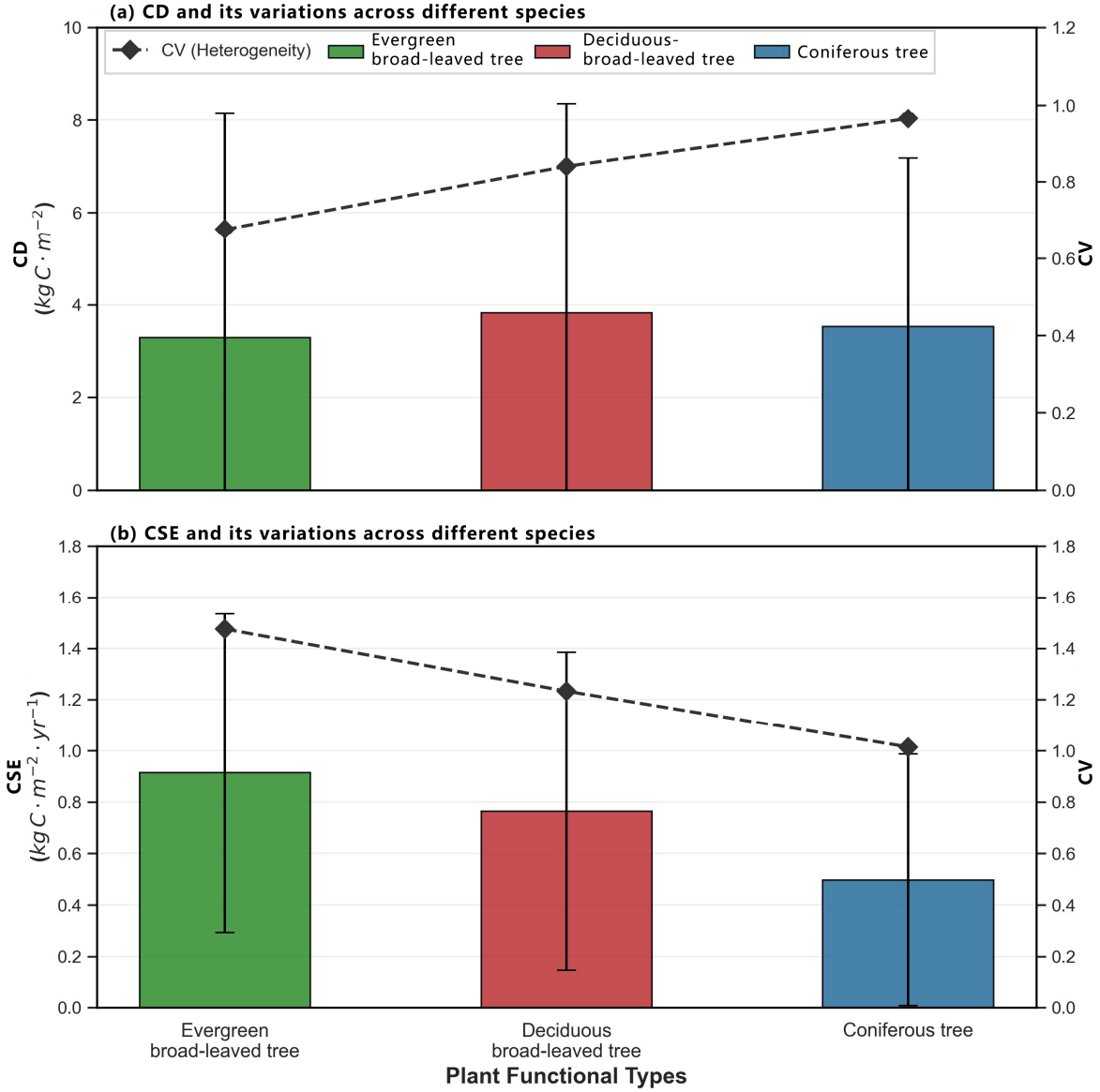

Figure 8. Variations in CD and CSE across different tree species. (**a**) Variations in CD across tree species and (**b**) variations in CSE across tree species. The colored bar charts display the mean values for each tree species. Error bars indicate the SD. The dashed lines on the secondary y-axis represent the CV to reflect the heterogeneity of carbon sequestration capacity among tree species.

Deciduous broadleaved trees constituted the structural backbone of the urban forest carbon storage. Despite seasonal dormancy, they exhibited the highest CD (3.82 kg C · m^{-2}), suggesting that these species—often older or possessing higher wood density—prioritize long-term biomass accumulation. In contrast, Evergreen broadleaved trees demonstrated a "high-flux" strategy. Although their carbon stock was lower, they outperformed other types in CSE (0.91 kg C · m^{-2} · yr^{-1}). This functional advantage is likely attributed to their extended phenological activity, allowing for continuous photosynthesis and carbon uptake throughout the year, unlike their deciduous counterparts. Coniferous trees, conversely, displayed the most conservative growth strategy, maintaining moderate carbon stocks but significantly lower CSE (0.50 kg C · m^{-2} · yr^{-1}), reflecting the slower physiological growth rates typical of gymnosperms in this climatic zone.

Furthermore, heterogeneity analysis (CV) highlighted distinct interspecific variations. While Evergreen broadleaved trees achieved the highest efficiency, they also exhibited the greatest instability in performance (CV_CSE = 1.48). This high variability suggests that carbon sequestration within this group is highly species-dependent or sensitive to micro-environmental conditions. Conversely, Deciduous and Coniferous trees showed relatively lower variability (CV < 1.25), indicating more predictable carbon service delivery across different species within these groups. These patterns underscore the importance of diverse species configurations: deciduous trees provide a stable carbon reservoir, while evergreen species offer rapid, albeit variable, annual carbon remediation.

3.2. Functional Classification of Carbon Sink Capability

We applied hierarchical cluster analysis to categorize the carbon sink capability of 153 tree species. This classification distinguishes species based on their balance between carbon storage and carbon sequestration, providing a functional basis for selecting high-performance urban vegetation (Figures A1–A3).

3.2.1. Evergreen Broadleaved Trees

The analysis classified the 25 evergreen broadleaved species into four functional roles (Figure A1). The majority of these species (20 out of 25, Group I) displayed consistent moderate to high capabilities in both storage and sequestration. This indicates that evergreen broadleaved trees generally serve as the reliable backbone of urban carbon sinks. Among the outliers, widely planted species like *Cinnamomum camphora* (Group II) acted as major reservoirs due to their high biomass accumulation. Conversely, *Phyllostachys edulis* (Group IV) represented a unique fast-response strategy characterized by high sequestration efficiency despite low standing stock.

3.2.2. Deciduous Broadleaved Trees

Functional differentiation among the 105 deciduous species was highly polarized (Figure A2). A dominant proportion comprising 59 species (Group I) exhibited the lowest carbon sink capability. This suggests that over half of the common deciduous landscape trees contribute minimally to direct carbon goals. On the other end of the spectrum, a small elite cluster of three species (Group IV: *Ginkgo biloba*, *Populus* × *canadensis*, *Platanus* × *acerifolia*) demonstrated superior capability in both storage and sequestration. These "dual-high" species are therefore critical candidates for maximizing carbon sinks, while the intermediate groups (Groups II and III) provide supplementary ecological functions rather than primary carbon benefits.

3.2.3. Coniferous Trees

Coniferous trees showed a similar trend of uneven performance where species selection is the deciding factor (Figure A3). Most sampled species (17 out of 23, Group I) showed

consistently low carbon metrics. Only two specific species in Group III (*Pinus elliottii* and *Taxodium ascendens*) distinguished themselves with high performance in both storage and flux. This implies that while conifers contribute to biodiversity, only a few specific types function as efficient carbon sinks in this urban context.

4. Discussion

4.1. Decoupling of Carbon Storage and Sequestration Across Scales

This study systematically compared CD and CSE across multiple spatial and biological scales, revealing that the two indicators often exhibit asynchronous patterns. Their decoupling uncovers temporal and functional trade-offs within urban vegetation systems.

4.1.1. Green Space Scale: Site Typology and Ecological Structure

Regional and comprehensive parks (e.g., Yuhuatai, Yuzui Wetland Park) generally exhibited both high CD and CSE. This performance appears driven by their extensive area, complex stratification, and intact community structures [25,26], which benefit from reduced disturbance. Conversely, plaza and affiliated spaces tended to show limited carbon function, potentially due to high impervious surface ratios and simplified vertical structures [27].

However, typology alone does not dictate performance; intra-type variability was significant. For example, the mountainous Qingliang Mountain Park outperformed the lakeside Yueya Lake Park, a difference likely attributable to superior vertical layering in the former. Similarly, older institutional sites like Sipalou Campus displayed stronger carbon metrics, highlighting the influence of vegetation legacy and site history [28,29]. These findings imply that carbon sink function is shaped by the interaction of spatial typology with specific ecological and social contexts [25]. Cluster analysis identified four functional zones, though these simplify complex realities:

- High-CD, High- CSE: Regional parks acting as both reservoirs and active sinks.
- Low-CD, High- CSE: Younger plantings or herbaceous patches with rapid uptake but limited storage.
- High-CD, Low- CSE: Mature communities where growth rates may have stabilized despite high biomass.
- Low-CD, Low-CSE: Areas with structural deficits suitable for enhancement.

A key finding is the divergence between stock and flux. Some plaza spaces showed low CD but relatively high CSE, consistent with younger, fast-growing vegetation that maintains high photosynthetic activity despite low accumulated biomass. In contrast, certain mature regional parks exhibited high CD but lower CSE, potentially reflecting growth saturation associated with aging [30].

4.1.2. Community Scale: Vertical Stratification and Composition

Vertical stratification appears to be a key factor influencing carbon metrics. Complex communities with tree–shrub–herb layers generally outperformed simple shrub or grass-dominated structures. This pattern is consistent with the hypothesis of niche complementarity, where multilayered canopies optimize resource partitioning [31]. While canopy trees largely determine total stock, mid- and understory layers likely contribute to overall sequestration efficiency through increased leaf area density. Notably, communities with mixed evergreen groundcovers stored more carbon than those with deciduous counterparts, suggesting that functional composition within layers matters alongside structural complexity [32].

Evergreen broadleaf forests demonstrated a tendency toward both high CD and CSE. This performance may reflect the compound benefits of year-round photosynthesis in subtropical climates. In comparison, deciduous communities, despite potentially high CD,

often exhibited lower annual CSE, likely constrained by seasonal dormancy. These trends align with observations that functional traits like leaf longevity and phenology regulate urban carbon budgets [33], although local maintenance practices (e.g., pruning, irrigation) may also confound these structural effects.

4.1.3. Species Scale: Functional Traits and Trade-Offs

At the species level, we observed a divergence between storage and sequestration capabilities among evergreen, deciduous, and coniferous groups. Deciduous broadleaved trees exhibited high sequestration rates relative to their storage, a pattern indicative of a "high-flux" strategy where rapid seasonal growth compensates for dormancy [34]. Conversely, conifers showed comparable storage but lower sequestration rates, consistent with the conservative growth strategies and lower specific leaf area typical of gymnosperms. Evergreen broadleaved trees occupied an intermediate functional niche, balancing moderate CSE with stable CD. This balance is likely attributable to their extended phenological activity.

However, variability within groups was significant, particularly among conifers (CV > 0.96). This high intraspecific variation implies that carbon performance might not be solely determined by functional type; rather, it likely reflects a complex interaction modulated by species-specific physiological adaptations, planting context, and age structure. This inference aligns with previous findings indicating that conifer growth in urban environments can fluctuate widely depending on environmental stressors such as soil compaction and light competition [35], while stand age remains a critical determinant of long-term biomass accumulation [36]. These results imply a functional trade-off: species maximizing rapid uptake (deciduous) may differ from those ensuring long-term retention (conifers). Consequently, urban planning relying on a single functional type may compromise either short-term mitigation or long-term storage goals.

Therefore, a strategic mix of deciduous trees, evergreens, and conifers can help cities optimize both temporal and spatial carbon performance. This approach is feasible and supported by recent studies demonstrating that increasing tree species richness in subtropical forests significantly enhances ecosystem carbon storage through niche complementarity [37]. From a practical perspective, urban planners can utilize these findings by adopting a zoning strategy that prioritizes fast-growing deciduous species in recreational areas for immediate carbon offset, while interplanting shade-tolerant evergreens and conifers in conservation zones to secure long-term storage. Furthermore, this multi-species strategy aligns with international guidelines on urban forestry [38,39] and can be adapted to existing regional plans by incorporating it into ongoing near-natural vegetation restoration projects.

4.2. Implications for Urban Green Space Management

Based on the observed carbon metrics, several strategies could be considered for enhancing urban carbon sinks, although their implementation must balance ecological goals with social functions and spatial constraints.

4.2.1. Optimize Green Space and Vegetation Types

Large-scale green spaces with complex topography (e.g., mountainous parks) and established institutional sites (e.g., campuses) demonstrated superior carbon capacity. This suggests that urban planning could benefit from preserving and expanding medium-to-large green patches, particularly in suburban or waterfront zones where space permits. For spatially constrained institutional areas (schools, hospitals), introducing multilayered vegetation may offer a pathway to enhance carbon density without requiring land expansion.

4.2.2. Enhancing Structural Complexity and Species Configuration

Three-layered structures comprising trees, shrubs, and groundcovers exhibit superior carbon performance. Mixed evergreen–deciduous and conifer–broadleaf forests were among the most efficient configurations identified. These findings are consistent with studies in cities like Zhengzhou and Beijing, which emphasize the structural regulation of carbon sink performance [40,41]. A recent meta-analysis further indicates that mixed-species stands can store up to 70% more carbon than monocultures [42].

Accordingly, design should prioritize vertically structured, multi-species plantings. In spatially constrained areas, fast-growing and high-efficiency carbon-fixing species should be combined. Single-layer lawns or shrublands should be avoided; vertical complexity can be enhanced through strategic integration of tree canopies or localized shrub islands.

4.2.3. Selection of High-Performance Species

Species such as *Pinus elliottii*, *Taxodium ascendens*, and *Cedrus deodara* demonstrated both high sequestration rates and substantial carbon storage, aligning with research in Vancouver showing superior carbon performance of mixed conifer–broadleaf forests [43]. These species represent strong candidates for framework planting in parks and greenways. In contrast, smaller ornamental species (e.g., *Malus halliana*) generally showed lower carbon benefits.

However, maximizing carbon storage should not be the sole criterion for species selection, as urban forests must deliver a broad spectrum of ecosystem services. For instance, ornamental species provide indispensable esthetic and cultural benefits that support mental well-being [44], while broadleaf species with complex canopies contribute significantly to ecological functions such as urban heat island mitigation and biodiversity conservation [45]. Therefore, we recommend a holistic selection framework that balances high carbon performers with species offering sensory and ecological benefits, ensuring that carbon goals do not compromise the social and environmental vitality of the city.

4.2.4. Strategies for Multi-Source LiDAR Data Acquisition

The integration of UAV and Backpack LiDAR systems requires balancing data completeness with acquisition efficiency. A critical factor determining the optimal deployment strategy is the canopy closure (CC) of the surveyed stand. Based on our field trials and data quality assessment, we observed a distinct threshold regarding the effectiveness of UAV LiDAR. In stands with low-to-moderate canopy density (CC < 70%), UAV LiDAR provided sufficient ground point density and stem detection rates, making it the preferred tool due to its high efficiency and top–down coverage. However, in high-density stands (CC > 70%), particularly during the leaf-on season, the occlusion effect significantly impeded the UAV laser pulses from penetrating to the understory. In these scenarios, the reliance solely on UAV data resulted in incomplete trunk reconstruction and large vertical blind spots.

Therefore, we strongly recommend a hybrid approach for such high-density areas by allocating approximately 60%–70% of the labor effort to ground-based (Backpack) acquisition. This strategy ensures the retrieval of accurate DBH and lower-canopy structure, while the UAV is used primarily for canopy top delineation. Furthermore, future inventories could benefit from pre-survey stratification using low-cost satellite imagery to identify these high-density zones where terrestrial scanning is mandatory, thereby optimizing the deployment of labor-intensive ground equipment.

4.3. Limitations and Future Research

While this study provides a multi-scale assessment of urban carbon dynamics, two primary limitations regarding estimation methods and temporal coverage should be acknowledged.

First, a recognized limitation of this study is the reliance on allometric equations derived primarily from natural forests or commercial plantations, as specific equations for urban trees in this region are currently scarce. Urban trees differ morphologically from their forest counterparts due to anthropogenic management and open-growth environments, which can introduce estimation errors [34,46]. To mitigate this uncertainty, we applied a strict selection protocol for the allometric equations: only equations developed for tree species within the same or similar climatic zones (subtropical monsoon climate) and geographic regions (East China) were utilized. This ensures that the biomass estimates reflect the local hydrothermal conditions and growth patterns to the greatest extent possible. Despite this precaution, the use of regional forest equations remains a necessary proxy in current urban carbon assessments [34]. Future research should aim to develop specific urban tree equations for this region to further improve accuracy.

Second, our assessment of CSE primarily reflects peak growing season dynamics. Since deciduous trees lack foliage in winter, accurately measuring their LAI and photosynthetic rates during the dormant season is structurally challenging. Consequently, our CSE calculations are based on leaf-on (summer) data, capturing the maximum potential sequestration but potentially overlooking the minimal respiratory fluxes or bark photosynthesis that occur in winter. While this approach effectively highlights functional differences during the active period, a complete annual carbon budget would require integrating multi-temporal physiological monitoring to fully quantify seasonal phenological variations.

Third, regarding methodological feasibility, the primary challenge lies in the massive data volume and high processing complexity associated with multi-source LiDAR. The integration of UAV and backpack systems generates high-density point clouds that require high-performance computing resources and specialized technical expertise for registration, denoising, and metric extraction. These requirements elevate the computational costs and technical threshold of the study [4]. However, compared to traditional manual field surveys—which are labor-intensive, time-consuming, and prone to human error—this approach represents a superior trade-off, achieving a critical balance between high-precision structural retrieval and operational speed [47].

Finally, it should be noted that this study is primarily designed as a plot-level inventory investigation. Our focus was on validating the methodological framework for fusing multi-platform LiDAR data and ensuring the accuracy of metric extraction. Consequently, the generation of continuous thematic maps and the analysis of the spatial heterogeneity of carbon storage across the entire landscape were not within the scope of this work. The upscaling of these high-precision plot-level estimates to a regional scale to enhance spatial interpretability remains a key objective for our future research.

5. Conclusions

This study applied a dual-platform LiDAR framework to quantify CD and CSE across 20 urban green spaces in Nanjing. The analysis revealed a divergence between carbon stock and flux metrics across multiple scales. Specifically, sites or communities with high biomass accumulation (high CD) did not necessarily exhibit high annual sequestration rates (high CSE), indicating distinct functional roles for different vegetation types.

The results demonstrate that community structure and composition significantly influence carbon outcomes. Multilayered communities containing mixed functional groups (e.g., conifer–broadleaf associations) exhibited simultaneous high values for both CD and CSE relative to single-layer monocultures. At the species level, functional differentiation was observed: deciduous broadleaved trees showed high seasonal sequestration rates, whereas coniferous species were characterized by lower turnover and stable long-term storage.

These findings suggest that urban carbon sink capacity is regulated by the interaction between vertical complexity and plant functional traits. Effective carbon management strategies, therefore, depend on balancing these structural and functional components—integrating fast-growing species for flux with long-lived species for storage—rather than maximizing a single metric. While constrained by the use of regional allometric equations and peak-season data, this research quantifies the structural heterogeneity of urban vegetation, providing empirical data to support structure-based green space planning.

Author Contributions: Conceptualization, Y.F. and Y.C. (Yuning Cheng); methodology, Y.F. and W.S.; software, Y.F. and S.S.; validation, Y.F. and Y.C. (Yilun Cao); formal analysis, Y.F. and W.S.; investigation, Y.F., W.S. and Y.C. (Yilun Cao); resources, Y.F.; data curation, Y.F. and S.S.; writing—original draft preparation, Y.F.; visualization, Y.F. and W.S.; supervision, Y.C. (Yuning Cheng); project administration, Y.C. (Yuning Cheng); funding acquisition, Y.C. (Yuning Cheng). All authors have read and agreed to the published version of the manuscript.

Funding: This research was funded by the Key Program of the National Natural Science Foundation of China, grant number 51838003, which provided sufficient financial support.

Data Availability Statement: Data will be made available upon request.

Conflicts of Interest: The authors declare no conflicts of interest.

Abbreviations

The following abbreviations are used in this manuscript:

Carbon sequestration	CSeq
Carbon sequestration efficiency	CSE
Carbon storage	CS
Carbon density	CD
Carbon fraction	CF
Root-to-Shoot Ratio	RSR
Diameter at Breast Height	DBH
Canopy height	CH
Crown Width	CW
Crown area	CA
Leaf Area Index	LAI
Net photosynthetic rate	NPR
Net assimilation rate	NAR
Biomass	B
Green area	GA
EB	Evergreen Broadleaf Forest
DB	Deciduous Broadleaf Forest
EC	Evergreen Coniferous Forest
DC	Deciduous Coniferous Forest
EDCM	Evergreen-Deciduous Conifer Mixed Forest
EDBM	Evergreen-Deciduous Broadleaf Mixed Forest
EDCBM	Evergreen-Deciduous Conifer-Broadleaf Mixed Forest
ES	Evergreen shrub
CS	Deciduous shrub
MS	Mixed shrub
EG	Evergreen groundcover
DG	Deciduous groundcover
MG	Mixed groundcover
Standard Deviation	SD
Coefficient of Variation	CV

Appendix A

Table A1. Sample site selection and number of communities.

Type of Green Space		Name of Green Space	No.	Number of Communities
Park green space	Comprehensive Park (waterfront)	Xuanwu Lake Park	1	60
		Mochou Lake Park	2	30
		Crescent Lake Park	3	20
		Xiuqiu Park	4	20
		Little Peach Park	5	20
	Comprehensive Park (Mountain)	Qingliang mountain-Stone city Park	6	30
		Arctic Pavilion Park	7	20
	Neighborhood park	Peace Park	8	5
	Specialty park	Hexi Qingao Forest Park (other specialized parks)	9	30
		Nanjing China Greening Expo Park (other specialized parks)	10	35
		Hexi Ecological Park (other specialized parks)	11	30
		Xi'anmen Ruins Park (Ruins Specialized Park)	12	15
Plaza green space		Daxinggong Civic Plaza	13	5
		Drum Tower Plaza	14	10
Affiliated green space	Campus	Jiulonghu Campus of Southeast University	15	20
		Sipalou Campus of Southeast University	16	10
	Commercial	Jinling Riverside Hotel	17	15
	Residential	Cui Ping Dong Nan	18	20
Regional green space	Scenic	Yuhuatai Scenic Area	19	20
	Wetlands	Fish Mouth Wetland Park	20	30

Table A2. Root-stem ratio (RSR) and carbon fraction (CF) of common vegetation in Nanjing.

Types	RSR	CF	Types	RSR	CF
Pinus sylvestris var. *mongolica*	0.236	0.486	*Betula platyphylla*	0.236	0.506
Pinus yunnanensis	0.236	0.508	*Eucalyptus* spp.	0.226	0.525
Pinus kesiya var. *langbianensis*	0.236	0.501	*Firmiana simplex*	0.236	0.423
Pinus elliottii	0.236	0.474	*Platanus* × *acerifolia*	0.236	0.441
Pinus massoniana	0.236	0.525	*Acer* spp.	0.236	0.45
Larix gmelinii	0.236	0.489	*Ginkgo biloba*	0.236	0.447
Pinus hwangshanensis	0.236	0.506	*Sapindus mukorossi*	0.236	0.435

Table A2. *Cont.*

Types	RSR	CF	Types	RSR	CF
Pinus taeda	0.284	0.511	*Koelreuteria paniculata*	0.236	0.424
Pinus armandii	0.174	0.523	*Celtis sinensis*	0.236	0.422
Pinus densata	0.235	0.501	*Liquidambar formosana*	0.236	0.418
Pinus koraiensis	0.215	0.511	*Bischofia polycarpa*	0.236	0.436
Pinus thunbergii	0.28	0.515	*Schima superba*	0.236	0.471
Pinus tabuliformis	0.236	0.517	*Michelia chapensis*	0.236	0.443
Pinus densiflora	0.236	0.515	*Alnus trabeculosa*	0.236	0.45
Cedrus deodara	0.236	0.454	*Populus tomentosa*	0.236	0.471
Quercus spp.	0.153	0.48	*Populus* spp.	0.236	0.43
Betula spp.	0.212	0.487	*Salix matsudana*	0.236	0.432
Picea spp.	0.236	0.49	*Salix* spp.	0.236	0.465
Abies spp.	0.181	0.496	*Ulmus* spp.	0.236	0.421
Cryptomeria fortunei	0.236	0.514	*Sophora japonica*	0.236	0.444
Metasequoia glyptostroboides	0.236	0.439	*Robinia* spp.	0.236	0.502
Cunninghamia lanceolata	0.236	0.446	*Prunus salicina*	0.236	0.44
Sabina chinensis	0.236	0.45	*Prunus* spp.	0.236	0.46
Cunninghamia lanceolata	0.236	0.499	*Prunus armeniaca*	0.236	0.43
Cupressus spp.	0.365	0.485	*Pyrus* spp.	0.236	0.46
Tilia spp.	0.201	0.475	*Syringa* spp.	0.236	0.43
Machilus pingii	0.199	0.485	*Malus* spp.	0.236	0.45
Cinnamomum spp.	0.236	0.434	*Forsythia* spp.	0.236	0.43
Magnolia spp.	0.236	0.434	*Broadleaf* species	0.236	0.48
Osmanthus fragrans	0.236	0.434	*Coniferous* species	0.236	0.489
Fraxinus chinensis	0.236	0.488			

Table A3. Leaf area index (LAI) and net photosynthetic rate (NPR) of common vegetation in Nanjing area.

Species	LAI	NPR	Species	LAI	NPR
Evergreen broadleaved tree			Evergreen scrub		
Cinnamomum camphora	3.04	13.66	*Fatsia japonica*	5.18	6.35
Cinnamomum glanduliferum	2.55	13.66	*Buxus sinica*	4.25	13.31
Cinnamomum burmanni	2.31	13.66	*Buxus microphylla*	4.25	13.31
Phoebe zhennan	3.26	6.2	*Buxus harlandii*	4.25	13.31
Trachycarpus fortunei	2.31	2.81	*Buxus microphylla* var. *variegata*	4.66	13.31
Michelia maudiae	2.01	6.73	*Euonymus alatus*	4.66	4.23
Michelia chapensis	2.01	6.73	*Euonymus japonicus*	4.66	4.23
Michelia alba	2.13	6.73	*Pittosporum tobira*	4.33	15.2
Magnolia grandiflora	4.878	11.714	*Rhododendron pulchrum*	3.97	12.74
Ilex chinensis	3.6	6.27	*Rhododendron simsii*	3.97	12.74
Photinia serratifolia	1.67	13.51	*Rhododendron indicum*	3.97	12.74
Eriobotrya japonica	3.6	3.13	*Camellia japonica*	1.96	4.22
Ardisia crenata	3.71	10.85	*Camellia sinensis*	3.5	3.35
Myrica rubra	2.89	2.81	*Camellia oleifera*	3.5	3.35
Vitex negundo var. *cannabifolia*	2.43	1.196	*Camellia sasanqua*	3.5	3.35
Elaeocarpus decipiens	1.494	6.985	*Aucuba japonica* 'Variegata'	5.67	5.56
Ligustrum lucidum	2.16	11.61	*Mahonia fortunei*	4.61	3.79
Osmanthus fragrans	3.53	8.13	*Mahonia bealei*	4.61	3.79
Osmanthus fragrans var. *thunbergii*	3.53	8.13	*Jasminum mesnyi*	2.51	3.88
Cyclobalanopsis glauca	1.85	10.66	*Ligustrum japonicum*	2.28	2.57
Lithocarpus glaber	1.85	15.27	*Ligustrum sinense* 'Silver Star'	2.28	4.325
Acer cinnamomifolium	1.57	3.85	*Gardenia jasminoides*	2.49	2.08
Citrus reticulata	2.25	7.66	*Serissa japonica*	3.25	3.82

Table A3. *Cont.*

Species	LAI	NPR	Species	LAI	NPR
Citrus medica	2.25	7.66	*Loropetalum chinense* var. *rubrum*	4.89	7.4
Phyllostachys edulis	1.25	6.7	*Loropetalum chinense*	4.89	7.4
Deciduous broadleaved tree			*Pyracantha fortuneana*	1.98	7.74
Platanus × *acerifolia*	2.23	4.04	*Elaeagnus pungens*	4.33	5.17
Sassafras tzumu	2.55	8.9	*Ilex crenata*	1.242	6.2
Lindera glauca	3.22	8.9	*Ilex cornuta*	4.49	4.97
Lindera benzoin	1.63	8.9	*Hypericum monogynum*	3.36	4.13
Ginkgo biloba	2.27	9.34	*Nandina domestica*	2.04	3.75
Triadica sebifera	2.06	8.71	*Yucca gloriosa*	2.31	4.53
Bischofia polycarpa	2.06	8.71	*Yucca filamentosa*	2.31	4.53
Sapindus mukorossi	1.09	11.72	*Michelia figo*	4.23	3.65
Koelreuteria paniculata	3.2	15	*Nerium oleander*	2.06	5.57
Koelreuteria bipinnata	3.2	15	*Vinca major* 'Variegata'	4.32	5
Acer mono	1.57	13.46	*Vinca major*	4.32	5
Acer buergerianum	2.73	13.459	*Juniperus sabina*	1.91	2.46
Acer truncatum	1.57	13.46	*Ficus pumila*	4.32	2.63
Acer palmatum var. dissectum	1.74	13.46	*Rhapis excelsa*	1.95	3.65
Aesculus chinensis	2.66	6.53	*Vaccinium bracteatum*	4.33	5.17
Liriodendron chinense	1.91	8.519	*Cycas revoluta*	1.95	0.82
Magnolia denudata	2.13	8.05	*Phyllostachys aureosulcata*	1.84	3.61
Magnolia × *soulangeana*	2.13	13.55	*Pleioblastus fortunei*	1.84	3.61
Magnolia liliflora	2.134	7.159	*Indocalamus tessellatus*	1.84	3.61
Salix babylonica	3.88	18.78	*Bambusa multiplex*	1.84	3.61
Salix alba	3.88	18.78	*Phyllostachys violascens*	1.84	3.61
Salix matsudana 'Pendula'	2.052	18.783	Deciduous scrub		
Salix matsudana	1.6	18.78	*Sambucus chinensis*	2.18	8.53
Populus × *canadensis*	3.88	11.149	*Lonicera maackii*	1.47	8.53
Populus tomentosa	3.88	11.149	*Lonicera japonica*	1.47	8.53
Celtis sinensis	1.46	8.206	*Abelia chinensis*	1.47	8.53
Zelkova schneideriana	2.7	4.216	*Weigela florida*	1.47	8.53
Ulmus pumila	2.07	10.95	*Cytisus scoparius*	2.18	4.8
Ulmus parvifolia	2.04	12.03	*Wisteria sinensis*	2.12	4.8
Prunus serrulata 'Kanzan'	1.71	5.36	*Forsythia suspensa*	2.28	3.88
Prunus serrulata 'Somei-yoshino'	1.17	5.62	*Forsythia* × *intermedia*	4.32	11.3
Prunus serrulata	1.95	5.62	*Jasminum nudiflorum*	4.32	11.3
Prunus speciosa	1.95	5.62	*Ligustrum* × *vicaryi*	2.28	2.57
Prunus jamasakura	1.34	5.42	*Ligustrum quihoui*	2.28	2.57
Prunus × *blireiana*	1.95	4.54	*Ligustrum ovalifolium*	2.28	2.57
Amygdalus davidiana	1.422	6.83	*Ligustrum sinense* 'Variegatum'	2.28	2.57
Prunus persica 'Versicolor'	1.422	6.83	*Ligustrum sinense*	2.28	4.325
Prunus persica f. atropurpurea	1.422	5.53	*Ligustrum lucidum*	2.28	3.325
Prunus persica 'Pendula'	1.422	5.53	*Spiraea* × *vanhouttei*	2.69	5.9
Prunus armeniaca	1.422	5.53	*Spiraea salicifolia*	2.69	5.9
Prunus persica	1.422	5.53	*Spiraea prunifolia*	2.69	5.9
Prunus persica 'Chrysanthemum'	1.422	5.53	*Rosa rugosa*	3.36	4.25
Prunus cerasifera 'Atropurpurea'	3.24	4.19	*Rosa chinensis*	4.36	4.25
Prunus mume	1.95	5.36	*Rosa multiflora*	6.36	4.25
Prunus triloba	1.95	5.36	*Kerria japonica*	5.36	4.25
Crataegus pinnatifida var. *major*	1.422	5.53	*Photinia* × *fraseri*	3.46	13.51
Malus spectabilis	1.7	4.54	*Paeonia suffruticosa*	8.36	7.88
Malus halliana	1.7	4.54	*Hydrangea macrophylla*	1.62	3.5
Malus hupehensis	1.7	4.54	*Berberis thunbergii* 'Atropurpurea'	2.69	5.9
Malus micromalus	1.7	4.54	*Berberis thunbergii*	2.69	5.9
Chaenomeles speciosa	1.94	6.82	*Cornus alba*	2.69	10.25

Table A3. *Cont.*

Species	LAI	NPR	Species	LAI	NPR
Chaenomeles sinensis	2.89	4.54	*Sanguisorba officinalis*	2.69	8.5
Pyrus bretschneideri	2.03	6.15	*Plumeria rubra*	2.69	5.57
Crataegus pinnatifida	2.14	6.23	Annual or biennial herbaceous ground cover		
Gleditsia sinensis	3.9	18.07	*Bromus inermis*	0.92	6.69
Robinia pseudoacacia	4.5	18.07	*Poa pratensis*	0.92	6.69
Sophora japonica	2.61	18.07	*Stellaria media*	0.92	6.69
Sophora japonica 'Golden Stem'	1.386	18.07	*Cerastium glomeratum*	0.92	6.69
Sophora japonica 'Pendula'	2.67	15.72	*Parthenocissus tricuspidata*	0.92	6.69
Albizia julibrissin	1.86	6.13	*Bidens pilosa*	0.92	6.69
Pterocarpus indicus	1.86	6.13	*Coreopsis tinctoria*	0.92	6.69
Cercis chinensis	1.92	7.57	*Conyza canadensis*	0.92	6.69
Melia azedarach	2.89	5.63	*Brassica napus*	0.92	6.69
Toona sinensis	4.3	5.63	*Orychophragmus violaceus*	0.84	8.55
Acer rubrum	3.93	5.02	*Veronica arvensis*	0.92	6.69
Acer spp.	5.27	5.02	*Veronica persica*	0.92	6.69
Acer palmatum	1.85	5.02	*Corydalis yanhusuo*	0.92	6.69
Firmiana simplex	3.43	17.03	*Papaver rhoeas*	0.92	6.69
Hibiscus mutabilis	1.84	5.98	*Primula* spp.	0.92	6.69
Hibiscus syriacus	1.84	5.98	*Astragalus sinicus*	0.92	6.69
Lagerstroemia indica	2.33	16.96	*Brassica oleracea*	0.92	6.69
Punica granatum	1.94	4.88	*Capsella bursa-pastoris*	0.92	6.69
Ailanthus altissima	3.132	16.42	Perennial herbaceous groundcover		
Liquidambar formosana	1.602	4.984	*Ophiopogon japonicus*	0.92	6.69
Morus alba	1.99	3.73	*Liriope platyphylla*	1.3	11.13
Broussonetia papyrifera	2.062	8.73	*Ophiopogon bodinieri*	0.92	6.69
Cudrania tricuspidata	2.062	8.73	*Hosta plantaginea*	0.92	6.69
Pterocarya stenoptera	1.926	12.4	*Aspidistra elatior*	0.92	6.69
Carya cathayensis	1.26	4.24	*Aspidistra* spp.	0.92	6.69
Juglans regia	1.26	4.24	*Agave americana*	0.92	6.69
Juglans nigra	1.26	4.24	*Reineckea carnea*	0.92	4.02
Pistacia chinensis	1.57	4.197	*Tulipa gesneriana*	0.92	6.69
Sapindus delavayi	1.57	12.6	*Ophiopogon japonicus 'Variegatus'*	0.92	11.13
Alangium chinense	1.22	5.591	*Oxalis corniculata*	0.92	6.69
Cornus officinalis	2.18	11.9	*Oxalis corymbosa*	0.92	6.69
Quercus acutissima	1.85	7.402	*Trifolium repens*	0.92	6.69
Quercus variabilis	4.16	7.402	*Medicago sativa*	0.92	6.69
Paulownia fortunei	1.8	20.81	*Lolium perenne*	0.92	6.69
Paulownia tomentosa	1.8	20.81	*Cynodon dactylon*	1.2	5.2
Diospyros kaki	3.71	10.12	*Phragmites australis*	0.92	6.69
Eucommia ulmoides	2.66	16.91	*Cortaderia selloana*	0.92	6.69
Catalpa bungei	2.46	7.44	*Arundo donax*	0.93	17.5
Tilia miqueliana	3.25	9.15	*Stipa capillata*	0.92	6.69
Ziziphus jujuba	2.74	11.88	*Miscanthus sinensis*	0.92	6.69
Syringa oblata	1.97	12.5	*Zephyranthes candida*	0.92	6.69
Euonymus bungeanus	2.32	8.63	*Lycoris radiata*	0.92	6.69
Davidia involucrata	4.18	7.15	*Allium victorialis*	0.92	6.69
Camptotheca acuminata	2.7	7.27	*Dianthus chinensis*	0.92	6.69
Zanthoxylum bungeanum	2.57	11.13	*Euonymus fortunei*	0.92	6.69
Viburnum macrocephalum	1.51	11.9	*Trachelospermum jasminoides*	0.92	6.69
Viburnum dilatatum	2.18	11.9	*Dichondra repens*	0.92	6.69
Chimonanthus praecox	4.72	4.36	*Iris tectorum*	0.75	4.63
Vitex negundo	1.84	5.98	*Iris germanica*	0.92	4.63
Hydrangea paniculata	2.18	11.9	*Artemisia argyi*	0.92	6.69
Edgeworthia chrysantha	1.84	2.99	*Anemone tomentosa*	0.92	6.69

Table A3. *Cont.*

Species	LAI	NPR	Species	LAI	NPR
Coniferous tree			*Jacobaea maritima*	0.92	6.69
Pinus bungeana	2.02	3.96	*Bellis perennis*	0.92	6.69
Pinus thunbergii	3.4	3.97	*Acorus calamus*	0.92	6.69
Pinus massoniana	1.31	6.39	*Campsis grandiflora*	0.92	6.69
Pinus tabuliformis	2.02	3.91	*Viola philippica*	0.92	6.69
Pinus parviflora	2.02	2.13	*Viola tricolor*	0.92	6.69
Cedrus deodara	3.11	10.778	*Viola cornuta*	0.92	6.69
Larix gmelinii var. *principis-rupprechtii*	2.23	3.58	*Hydrocotyle vulgaris*	0.92	6.69
Pinus elliottii	3.33	4.6	*Rosmarinus officinalis*	0.92	6.69
Pinus taeda	3.33	2.52	*Hydrocotyle sibthorpioides*	0.92	6.69
Picea pungens 'Glauca'	4.626	1.7	*Petunia hybrida*	0.92	6.69
Cunninghamia lanceolata	1.89	3.45	*Woodwardia japonica*	0.92	6.69
Taxodium ascendens	4.626	8.5	*Ipomoea cairica*	0.92	6.69
Taxodium distichum	5.34	8.5	*Canna indica*	0.92	6.69
Metasequoia glyptostroboides	3.34	8.5	*Juncus effusus*	0.92	6.69
Juniperus chinensis 'Kaizuka'	4.59	4.71	*Begonia semperflorens*	0.92	6.69
Juniperus formosana	3.88	4.71	*Sedum lineare*	0.92	6.69
Juniperus chinensis 'Pfitzeriana Aurea'	4.23	4.71	*Hemerocallis fulva*	0.92	6.69
Cupressus funebris	2.484	1.47	*Paeonia lactiflora*	0.92	6.69
Cryptomeria japonica	2.58	5.25			
Cryptomeria fortunei	2.58	5.25			
Platycladus orientalis	4.35	1.89			
Podocarpus macrophyllus	1.77	2.46			
Torreya grandis	1.89	5.05			

Table A4. The growth equations of common trees in Nanjing area with different speeds.

Species	Aboveground Biomass (kg)	Belowground Biomass (kg)	Whole Tree Biomass (kg)	Modeling Area
Cupressus funebris	$B_g = 0.02479D^{2.0333}$	$B_{ug} = 0.0261D^{2.1377}$		Jiangsu
Pinus thunbergii	$B_g = 0.0462(D^2H)^{0.9446}$	$B_{ug} = 0.0064(D^2H)^{1.0427}$		Anhui
Pinus massoniana	$B_{g2} = 0.06H^{0.7934}D^{1.8005}$ $B_{g3} = 0.137708H^{1.487266}L^{0.405207}$	$B_{ug} = 0.0417D^{2.2618}H^{-0.078}$	$B = B_{g2} + B_{g3} + B_{ugi}$	Zhejiang
Cunninghamia lanceolata	$B_{g2} = 0.0647H^{0.8959}D^{1.488}$ $B_{g3} = 0.097D^{1.7814}L^{0.0346}$	$B_{ug} = 0.061D^{2.115252}H^{-0.10374}$	$B = B_{g2} + B_{g3} + B_{ugi}$	Zhejiang
Cryptomeria fortunei		$B_{ugi} = 10.329 + 0.009D^2H$	$B = 38.665 + 0.055D^2H$	Jiangsu
Metasequoia glyptostroboides		$B_{ug} = 0.522 + 0.006D^2H$	$B = -5.826 + 0.047D^2H$	Jiangsu
Cinnamomum camphora	$B_g = 0.00751(D^2H)^{1.2675}$	$B_{ug} = 0.00268(D^2H)^{1.21846}$		Shanghai
Robinia pseudoacacia	$B_g = 0.0681(D^2H)^{0.9865} + 12.020 + 0.009(D^2H) - 0.549 + 0.007(D^2H) + 4.217 + 0.008(D^2H)$	$B_{ug} = 0.0087(D^2H)^{1.0513}$		Jiangsu
Elaeocarpus decipiens	$B_g = 0.00015(D^2H)^{1.28808}$	$B_{ug} = 0.01504(D^2H)^{1.10051}$		Shanghai

Table A4. *Cont.*

Species	Aboveground Biomass (kg)	Belowground Biomass (kg)	Whole Tree Biomass (kg)	Modeling Area
Quercus spp.	$B_g = 0.3108(D^2H)^{0.67428} + 0.0293(D^2H)^{0.75662} + 0.0922(D^2H)^{0.39445} + 0.93685(D^2H)^{0.614021}$	$B_{ug} = 0.1672284(D^2H)^{0.64106}$		Henan
Ulmus spp.	$B_g = 0.0709D^{2.42} + 4.924D^{0.976} + 1.163D^{0.64}$			Liaoning
Ligustrum lucidum	$B_g = 0.08685(D^2H)^{0.89923}$	$B_{ug} = 0.084559(D^2H)^{0.60667}$	$B = 0.02798(D^2H)^{0.91277}$	Shanghai
Magnolia grandiflora	$B_g = 0.08685(D^2H)^{0.89923}$	$B_{ug} = 0.088406(D^2H)^{0.67152}$		Shanghai
Hard broadleaf species/*Hardwood species*	$B_g = 0.03451(D^2H)^{1.0037}$	$B_{ug} = 0.0549H^{0.1068}D^{2.0953}$		Zhejiang
Populus spp.	$B_g = 0.0074046(D^2H)^{1.069} + 0.0041773(D^2H)^{0.9911} + 0.071532(D^2H)^{0.4489}$	$B_{ug} = 0.055106(D^2H)^{0.7061}$		Jiangsu
Paulownia spp.	$B_g = 0.01693(D^2H)^{0.9234} + 0.00247(D^2H)^{1.0977} + 0.145(D^2H)^{0.7156} + 0.004105(D^2H)^{0.9296}$	$B_{ug} = 0.06457(D^2H)^{0.6966}$	$B = 0.0574(D^2H)^{0.8925}$	Anhui
Koelreuteria bipinnata	$B_g = 0.02173(D^2H)^{1.08777}$	$B_{ug} = 0.01026(D^2H)^{1.02029}$		Shanghai
Liriodendron chinense	$B_g = 0.00950(D^2H)^{1.7994}$	$B_{ug} = 0.01755(D^2H)^{0.86672}$	$B = 0.00392(D^2H)^{1.20113}$	Shanghai
Soft broadleaf species/*Softwood broadleaves*	$B_{g2} = 0.044H^{0.7197}D^{1.7095}$ $B_{g3} = 0.0856D^{1.22657}L^{0.3970}$	$B_{ug} = 0.0417D^{2.0247}H^{-0.1067}$	$B = B_{g2} + B_{g3} + B_{ug}$	Zhejiang
Eucommia ulmoides	$B_g = 0.118194D^{2.047788} + 0.013137D^{2.919738} + 0.033970D^{0.001548}$			Henan
Ginkgo biloba	$B_g = 0.118604(D^2H)^{0.8237}$	$B_{ug} = 0.092321(D^2H)^{0.6799}$	$B = 0.033713(D^2H)^{0.9072}$	Shanghai
Mixed broadleaf species	$B_g = 0.17322D^{2.3458}$			Guizhou
Phyllostachys edulis	$B_g = 0.0712(D^2H)^{0.7066}$	$B_{ug} = 0.0379(D^2H)^{0.5776}$		Shanghai
Prunus persica (D = ground diameter)	$B_g = 0.18241D^{2.0558}$	$B_{ug} = 0.0821D^{1.7652}$		Shanghai
Shrub cluster/Shrub layer			$B = 0.0417H^{0.5427}D^{1.0615}$	Zhejiang
Coniferous tree species/*Conifers*	$B_g = 0.0326335(D^2H)^{0.9472}$		$B = 0.0515232(D^2H)^{0.9212}$	National
Broadleaf tree species/*Broadleaves*	$B_g = 0.1191632(D^2H)^{0.8542}$		$B = 0.1021363(D^2H)^{0.8793}$	National

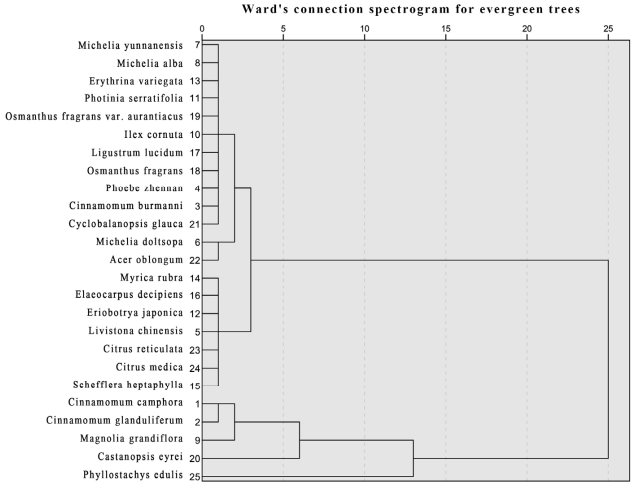

Figure A1. Cluster analysis of 25 evergreen broadleaf systems.

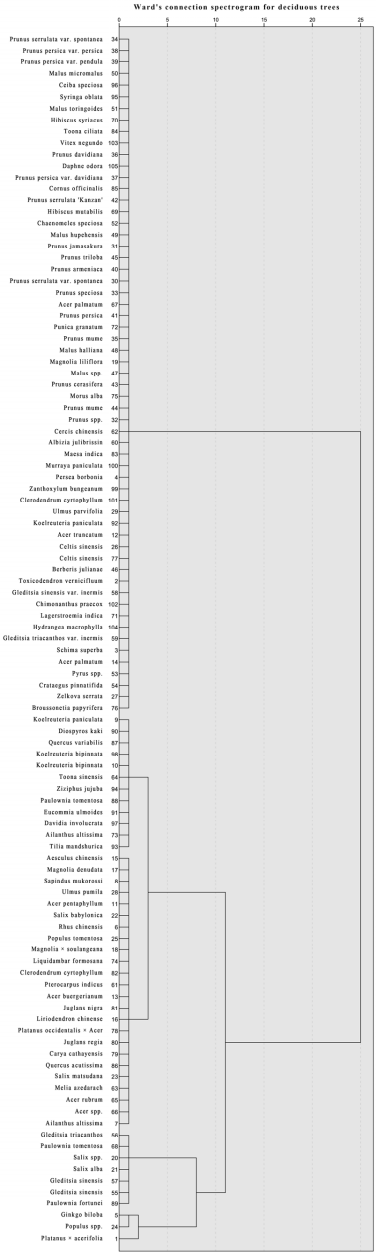

Figure A2. Cluster analysis of 105 deciduous broadleaf trees.

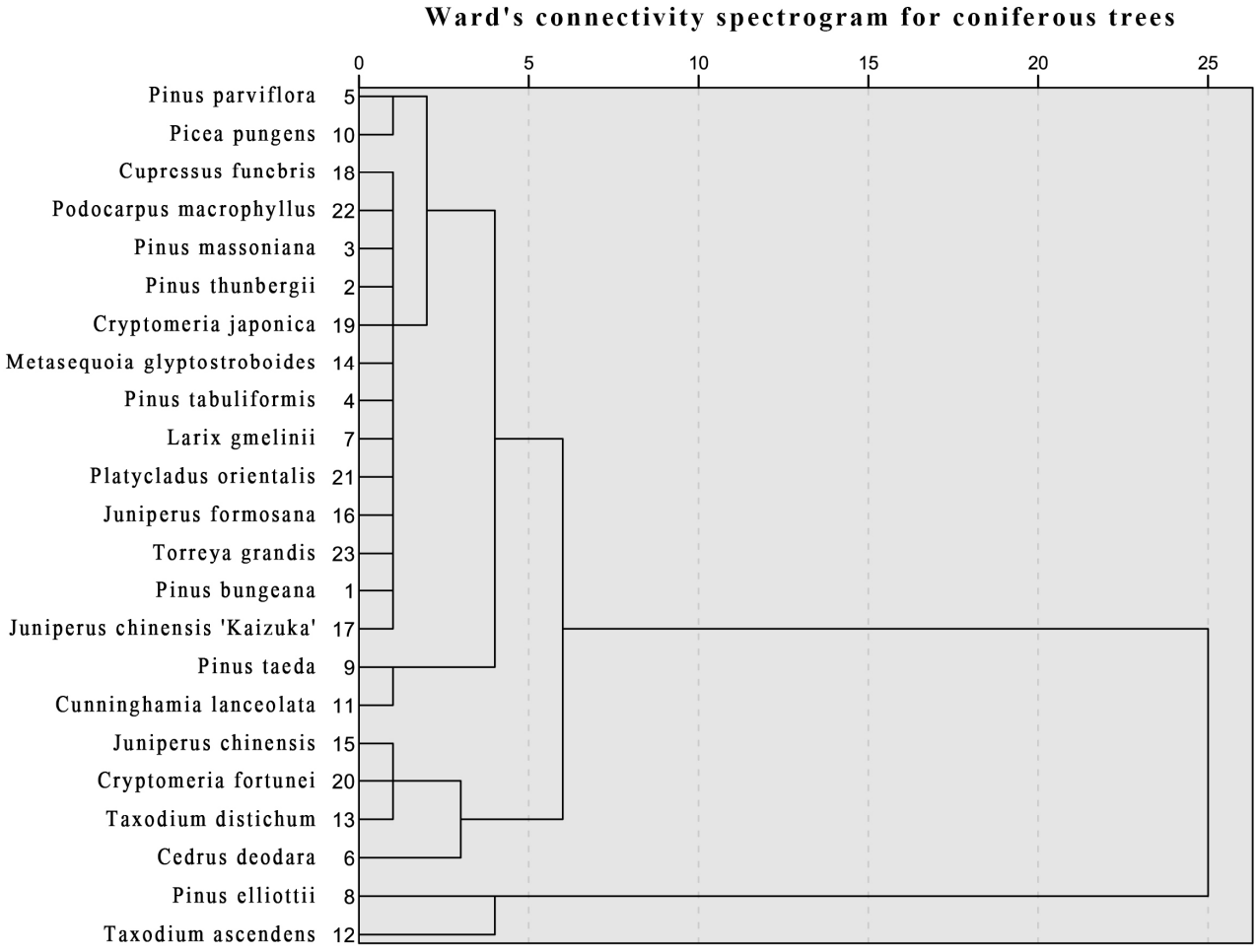

Figure A3. Cluster analysis of 23 species of coniferous trees.

References

1. Feng, Y.; Fang, C.; Jia, X.; Song, P.; Zhou, L.; Xu, X.; Wang, K.; He, R.; Guo, N.; Ge, S. Dual pathways of carbon neutrality in urban green spaces: Assessment and regulatory strategies. *Sustain. Cities Soc.* **2025**, *125*, 106311. [CrossRef]
2. Zhao, D.; Cai, J.; Xu, Y.; Liu, Y.; Yao, M. Carbon sinks in urban public green spaces under carbon neutrality: A bibliometric analysis and systematic literature review. *Urban For. Urban Green.* **2023**, *86*, 128037. [CrossRef]
3. Zhang, R.; Cheng, X.; Chen, W.; Lu, F.; Liu, S.; Shi, H.; Ni, Z.; Chen, Y.; Li, D.; Zhou, Y.; et al. Effects of different urban vegetation cover and green space types on soil greenhouse gas emissions and carbon sequestration. *Front. Environ. Sci.* **2025**, *13*, 1555628. [CrossRef]
4. Zhuang, Q.; Shao, Z.; Gong, J.; Li, D.; Huang, X.; Zhang, Y.; Xu, X.; Dang, C.; Chen, J.; Altan, O.; et al. Modeling carbon storage in urban vegetation: Progress, challenges, and opportunities. *Int. J. Appl. Earth Obs. Geoinf.* **2022**, *114*, 103058. [CrossRef]
5. Coops, N.C.; Irwin, L.A.; Seely, H.S.; Hardy, S.J. Advances in laser scanning to assess carbon in forests: From ground-based to space-based sensors. *Curr. For. Rep.* **2025**, *11*, 11. [CrossRef]
6. Timilsina, S.; Aryal, J.; Kirkpatrick, J.B. Mapping urban tree cover changes using object-based convolution neural network (OB-CNN). *Remote. Sens.* **2020**, *12*, 3017. [CrossRef]
7. Yang, M.; Zhou, X.; Liu, Z.; Li, P.; Tang, J.; Xie, B.; Peng, C. A review of general methods for quantifying and estimating urban trees and biomass. *Forests* **2022**, *13*, 616. [CrossRef]
8. Fang, Y.; Zhang, X.; Cao, Y. Digital technologies framework and future trends of carbon sequestration research in urban green spaces: A review. *Int. J. Environ. Sci. Technol.* **2025**, *22*, 13277–13296. [CrossRef]
9. Kleingeld, E.; van Hove, B.; Elbers, J.; Jacobs, C. Carbon dioxide fluxes in the city centre of Arnhem, A middle-sized Dutch city. *Urban Clim.* **2018**, *24*, 994–1010. [CrossRef]
10. Preston, P.D.; Dunk, R.M.; Smith, G.R.; Cavan, G. Examining regulating ecosystem service provision by brownfield and park typologies and their urban distribution. *Urban For. Urban Green.* **2024**, *95*, 128311. [CrossRef]
11. Musthafa, M.; Singh, G. Improving forest above-ground biomass retrieval using multi-sensor L-and C-band SAR data and multi-temporal spaceborne LiDAR data. *Front. For. Glob. Change* **2022**, *5*, 822704. [CrossRef]

12. Balestra, M.; Choudhury, M.A.M.; Pierdicca, R.; Chiappini, S.; Marcheggiani, E. UAV-Spherical Data Fusion Approach to Estimate Individual Tree Carbon Stock for Urban Green Planning and Management. *Remote Sens.* **2024**, *16*, 2110. [CrossRef]
13. Su, R.; Du, W.; Shan, Y.; Ying, H.; Rihan, W.; Li, R. Aboveground carbon stock estimation based on backpack LiDAR and UAV multispectral imagery at the forest sample plot scale. *Remote Sens.* **2024**, *16*, 3927. [CrossRef]
14. Mitchell, M.G.; Johansen, K.; Maron, M.; McAlpine, C.A.; Wu, D.; Rhodes, J.R. Identification of fine scale and landscape scale drivers of urban aboveground carbon stocks using high-resolution modeling and mapping. *Sci. Total Environ.* **2018**, *622–623*, 57–70. [CrossRef]
15. Yang, Z.; Fang, C.; Mu, X.; Li, G.; Xu, G. Urban green space quality in China: Quality measurement, spatial heterogeneity pattern and influencing factor. *Urban For. Urban Green.* **2021**, *66*, 127381. [CrossRef]
16. Wang, V.; Gao, J. Estimation of carbon stock in urban parks: Biophysical parameters, thresholds, reliability, and sampling load by plant type. *Urban For. Urban Green.* **2020**, *55*, 126852. [CrossRef]
17. Ellenberg, D.; Mueller-Dombois, D. *Aims and Methods of Vegetation Ecology*; Wiley: New York, NY, USA, 1974; Volume 547.
18. Nowak, D.; Crane, D.; Stevens, J.; Hoehn, R.; Walton, J.; Bond, J. A ground-based method of assessing urban forest structure and ecosystem services. *Arboric. Urban For.* **2008**, *34*, 347–358. [CrossRef]
19. Heo, H.K.; Lee, D.K.; Park, J.H.; Thorne, J.H. Estimating the heights and diameters at breast height of trees in an urban park and along a street using mobile LiDAR. *Landsc. Ecol. Eng.* **2019**, *15*, 253–263. [CrossRef]
20. Hirose, T.; Werger, M. Maximizing daily canopy photosynthesis with respect to the leaf nitrogen allocation pattern in the canopy. *Oecologia* **1987**, *72*, 520–526. [CrossRef] [PubMed]
21. Goudriaan, J. *Crop Micrometeorology: A Simulation Study*; Wageningen University and Research: Wageningen, The Netherlands, 1977.
22. Yao, X.; Ou, C.; Xia, L.; Yao, X.; Chen, Y.; Wang, N. Benefit evaluation of carbon sequestration, oxygen release, cooling and humidifying of the main landscape tree species in small towns along Huaihe River in Anhui Province. *Chin. J. Ecol.* **2021**, *40*, 1293.
23. Hyyppä, E.; Yu, X.; Kaartinen, H.; Hakala, T.; Kukko, A.; Vastaranta, M.; Hyyppä, J. Comparison of backpack, handheld, under-canopy UAV, and above-canopy UAV laser scanning for field reference data collection in boreal forests. *Remote Sens.* **2020**, *12*, 3327. [CrossRef]
24. Liang, X.; Kankare, V.; Hyyppä, J.; Wang, Y.; Kukko, A.; Haggrén, H.; Yu, X.; Kaartinen, H.; Jaakkola, A.; Guan, F.; et al. Terrestrial laser scanning in forest inventories. *ISPRS J. Photogramm. Remote Sens.* **2016**, *115*, 63–77. [CrossRef]
25. Huang, J.; Song, P.; Liu, X.; Li, A.; Wang, X.; Liu, B.; Feng, Y. Carbon Sequestration and Landscape Influences in Urban Greenspace Coverage Variability: A High-Resolution Remote Sensing Study in Luohe, China. *Forests* **2024**, *15*, 1849. [CrossRef]
26. Li, X.; Jiang, Y.; Liu, Y.; Sun, Y.; Li, C. The impact of landscape spatial morphology on green carbon sink in the urban riverfront area. *Cities* **2024**, *148*, 104919. [CrossRef]
27. Guo, Y.; Ren, Z.; Wang, C.; Zhang, P.; Ma, Z.; Hong, S.; Hong, W.; He, X. Spatiotemporal patterns of urban forest carbon sequestration capacity: Implications for urban CO2 emission mitigation during China's rapid urbanization. *Sci. Total Environ.* **2024**, *912*, 168781. [CrossRef] [PubMed]
28. Nayak, L.; Adavi, S.B.; Lal, P.; Behera, L.; Sahu, U.R.; Altaf, M.A.; Kumar, A.; Kumar, R.; Tiwari, R.K.; Lal, M.K. Urban Forests and Carbon Sequestration. In *Urban Forests, Climate Change and Environmental Pollution*; Springer: Cham, Switzerland, 2024; pp. 373–390.
29. Li, X.; Jia, B.; Li, F.; Ma, J.; Liu, X.; Feng, F.; Liu, H. Effects of multi-scale structure of blue-green space on urban forest carbon density: Beijing, China case study. *Sci. Total Environ.* **2023**, *883*, 163682. [CrossRef]
30. Francini, G.; Hui, N.; Jumpponen, A.; Kotze, D.J.; Setälä, H. Vegetation type and age matter: How to optimize the provision of ecosystem services in urban parks. *Urban For. Urban Green.* **2021**, *66*, 127392. [CrossRef]
31. Pregitzer, C.C.; Hanna, C.; Charlop-Powers, S.; Bradford, M.A. Estimating carbon storage in urban forests of New York City. *Urban Ecosyst.* **2022**, *25*, 617–631. [CrossRef]
32. Livesley, S.J.; McPherson, E.G.; Calfapietra, C. The urban forest and ecosystem services: Impacts on urban water, heat, and pollution cycles at the tree, street, and city scale. *J. Environ. Qual.* **2016**, *45*, 119–124. [CrossRef] [PubMed]
33. Bahrami, B.; Hildebrandt, A.; Thober, S.; Rebmann, C.; Fischer, R.; Samaniego, L.; Rakovec, O.; Kumar, R. Developing a parsimonious canopy model (PCM v1. 0) to predict forest gross primary productivity and leaf area index of deciduous broadleaved forest. *Geosci. Model Dev.* **2022**, *15*, 6957–6984. [CrossRef]
34. Nowak, D.J.; Greenfield, E.J.; Hoehn, R.E.; Lapoint, E. Carbon storage and sequestration by trees in urban and community areas of the United States. *Environ. Pollut.* **2013**, *178*, 229–236. [CrossRef] [PubMed]
35. Morgenroth, J.; Buchan, G.D. Soil moisture and aeration beneath pervious and impervious pavements. *Arboric. Urban For.* **2009**, *35*, 135–141. [CrossRef]
36. Stephenson, N.L.; Das, A.J.; Condit, R.; Russo, S.E.; Baker, P.J.; Beckman, N.G.; Coomes, D.A.; Lines, E.R.; Morris, W.K.; Rüger, N.; et al. Rate of tree carbon accumulation increases continuously with tree size. *Nature* **2014**, *507*, 90–93. [CrossRef]

37. Liu, X.; Trogisch, S.; He, J.; Niklaus, P.A.; Bruelheide, H.; Tang, Z.; Erfmeier, A.; Scherer-Lorenzen, M.; Pietsch, K.A.; Yang, B.; et al. Tree species richness increases ecosystem carbon storage in subtropical forests. *Proc. R. Soc. B* **2018**, *285*, 20181240. [CrossRef] [PubMed]
38. Pretzsch, H. Integrative Ecosystem Management Through the Diversification of Structure and Tree Species. In *Progress in Botany*; Springer: Cham, Switzerland, 2024; Volume 85, pp. 333–360.
39. Salbitano, F. *Guidelines on Urban and Peri-Urban Forestry*; FAO: Rome, Italy, 2016.
40. Wang, M.; Xu, H.; Zhao, J.; Sun, C.; Liu, Y.; Li, J. The Carbon Sequestration Potential of Skyscraper Greenery: A Bibliometric Review (2003–2023). *Sustainability* **2025**, *17*, 1774. [CrossRef]
41. Wang, Y.; Chang, Q.; Li, X. Promoting sustainable carbon sequestration of plants in urban greenspace by planting design: A case study in parks of Beijing. *Urban For. Urban Green.* **2021**, *64*, 127291. [CrossRef]
42. Warner, E.; Cook-Patton, S.C.; Lewis, O.T.; Brown, N.; Koricheva, J.; Eisenhauer, N.; Ferlian, O.; Gravel, D.; Hall, J.S.; Jactel, H.E.; et al. Young mixed planted forests store more carbon than monocultures—A meta-analysis. *Front. For. Glob. Change* **2023**, *6*, 1226514. [CrossRef]
43. Gülçin, D.; van den Bosch, C.C.K. Assessment of above-ground carbon storage by urban trees using LiDAR data: The case of a university campus. *Forests* **2021**, *12*, 62. [CrossRef]
44. Bratman, G.N.; Anderson, C.B.; Berman, M.G.; Cochran, B.; De Vries, S.; Flanders, J.; Folke, C.; Frumkin, H.; Gross, J.J.; Hartig, T.; et al. Nature and mental health: An ecosystem service perspective. *Sci. Adv.* **2019**, *5*, eaax0903. [CrossRef]
45. Ziter, C.D.; Pedersen, E.J.; Kucharik, C.J.; Turner, M.G. Scale-dependent interactions between tree canopy cover and impervious surfaces reduce daytime urban heat during summer. *Proc. Natl. Acad. Sci. USA* **2019**, *116*, 7575–7580. [CrossRef]
46. McHale, M.R.; Burke, I.C.; Lefsky, M.A.; Peper, P.J.; McPherson, E.G. Urban forest biomass estimates: Is it important to use allometric relationships developed specifically for urban trees? *Urban Ecosyst.* **2009**, *12*, 95–113. [CrossRef]
47. Gollob, C.; Ritter, T.; Nothdurft, A. Forest inventory with long range and high-speed personal laser scanning (PLS) and simultaneous localization and mapping (SLAM) technology. *Remote Sens.* **2020**, *12*, 1509. [CrossRef]

Disclaimer/Publisher's Note: The statements, opinions and data contained in all publications are solely those of the individual author(s) and contributor(s) and not of MDPI and/or the editor(s). MDPI and/or the editor(s) disclaim responsibility for any injury to people or property resulting from any ideas, methods, instructions or products referred to in the content.